FLANGE LOCAL BUCKLING RESISTANCE AND LOCAL-GLOBAL BUCKLING INTERACTION IN SLENDER-FLANGE WELDED I-SECTION BEAMS

A Dissertation
Presented to
The Academic Faculty

by

Wajahat Latif

In Partial Fulfillment
of the Requirements for the Degree
Master of Science in Civil Engineering in the
School of Civil and Environmental Engineering

Georgia Institute of Technology

May 2020

COPYRIGHT © 2020 BY WAJAHAT LATIF

FLANGE LOCAL BUCKLING RESISTANCE AND LOCAL-GLOBAL BUCKLING INTERACTION IN SLENDER-FLANGE WELDED I-SECTION BEAMS

Approved by:

Dr. Donald W. White, Advisor
School of Civil and Environmental Engineering
Georgia Institute of Technology

Dr. Lauren Stewart
School of Civil and Environmental Engineering
Georgia Institute of Technology

Dr. Ryan J. Sherman
School of Civil and Environmental Engineering
Georgia Institute of Technology

Date Approved: April 24, 2020

To my family, for their unconditional love and support

ACKNOWLEDGEMENTS

I would like to express my deepest gratitude to my advisor, Dr. Donald White, for giving me the opportunity to work with him and for his constant guidance and mentorship. I have found myself being inspired by his knowledge and his passion for research every day. His accessibility to his students, his patience with their concerns and his regard for their opinions nourishes their potential and proves to be a constant source of motivation. It has indeed been a huge honor to work with him and learn from his expertise.

I would also like to extend my gratitude to the rest of my committee members, Dr. Lauren Stewart and Dr. Ryan Sherman, for their valuable suggestions.

I would like to thank my fellow students, Ajit Kamath and Ryan Slein, for their help in this research.

I would also like to convey my sincere gratitude to the Fulbright Scholarship Program for funding my studies at Georgia Tech and making this possible.

The completion of this research work also marks the end of my master's degree and I would like to express my gratitude to everyone who has been a part of this journey, especially my teachers who have inspired me daily and my peers and friends who have made this experience worth the while.

I would especially like to thank my family for their unwavering love and support. Last, but not the least, I am thankful for my fiancé, Ayesha Ali, for being a constant source of happiness and strength in my life.

TABLE OF CONTENTS

LIST OF TABLES

LIST OF FIGURES

LIST OF SYMBOLS AND ABBREVIATIONS

A	Gross cross-sectional area
A_f	Area of flange
A_w	Area of web
A_e	Effective area of cross-section
C_b	Beam moment gradient and load height factor
D_{cy}	Depth of web in compression at the onset of yield at the compression flange
D_{cp}	Depth of web in compression for a fully-plastic cross-section
D_{ce}	Depth of web in compression for the effective section
E	Modulus of elasticity of steel
F_{el}	Elastic local buckling stress
F_y	Specified minimum yield stress
F_{yc}	Specified minimum yield stress of the compression flange
F_{yt}	Specified minimum yield stress of the tension flange
I_x	Moment of inertia about the major principal axis
I_{xe}	Moment of inertia about the major principal axis for the effective section
I_y	Moment of inertia about the minor principal axis
I_{yc}	Moment of inertia of the compression flange about the axis of the web
J	St. Venant torsional constant
L_b	Member unbraced length between the braced points
L_p	Beam unbraced length limit within which the AISC nominal lateral torsional buckling (LTB) resistance under uniform bending is equal to the plateau LTB resistance

L_r	Beam unbraced length limit beyond which the nominal AISC lateral torsional buckling (LTB) resistance is taken as the theoretical elastic LTB resistance
M_{max}	Largest potential moment that can be developed in the beam cross-section considering the three potential governing limit states of compression flange yielding, compression flange local buckling, and tension flange yielding
$M_{nFLB.max}$	Largest potential moment that can be developed in the beam cross-section considering only the compression flange local buckling limit state
M_n	Member nominal flexural strength
M_p	Cross-section plastic bending moment
M_{yc}	Moment at nominal yielding of the extreme fiber of the compression flange
M_{yce}	Moment at nominal yielding of the extreme fiber of the compression flange for the effective section
M_{yt}	Moment at first yielding of the compression flange
R_{pg}	AISC (2016) cross-section bend buckling strength reduction factor
R_{pge}	Cross-section bend buckling strength reduction factor for the effective section
R_{pc}	AISC (2016) web plastification factor, or effective plastic section modulus considering web slenderness effects
S_x	Elastic section modulus
S_{xc}	Elastic section modulus to the extreme fiber of the compression flange for major-axis bending
S_{xce}	Elastic section modulus to the extreme fiber of the compression flange for major-axis bending for an effective section
S_{xt}	Elastic section modulus to the extreme fiber of the tension flange for major-axis bending
b_f	Width of flange
h	Clear distance between the flanges
h_o	Distance between the flange centroids
h_{cy}	Twice the distance from the centroid of the cross-section to the inside face of the compression flange at the onset of yielding at the compression flange
r_t	Effective radius of gyration

t_f	Thickness of flange
λ_f	Flange width-to-thickness ratio
λ_{pf}	Limiting width-to-thickness parameter for compact flange
λ_{rf}	Limiting width-to-thickness parameter for noncompact flange
λ_w	Web width-to-thickness ratio
λ_{pw}	Limiting width-to-thickness parameter for compact web
λ_{rw}	Limiting width-to-thickness parameter for noncompact web
$\lambda_{rf.AISC}$	Limiting width-to-thickness parameter for noncompact flange per AISC (2016)
$\lambda_{rf.new}$	Limiting width-to-thickness parameter for noncompact flange corresponding to a location on the flange local buckling (FLB) curve where the full-width of the flange becomes fully effective
LTB	Lateral torsional buckling
FLB	Flange local buckling

SUMMARY

The AISC (2016) Specification idealizes the strength of slender-flange beams as the theoretical elastic plate local bucking strength. Recent research has shown that this idealization is highly conservative. There is a substantial post-buckling strength of slender flanges that is ignored in AISC (2016). As the use of slender flanges becomes more common, due to the use of higher strength steels and/or due to design optimization, there is a need to have a better characterization of their strength to improve their economy. Another important aspect not addressed in the AISC (2016) Specification's Chapter F is the potential interaction between local and global buckling in flexural members. This effect has been studied to only a limited extent in previous research and deserves more attention to ensure the behavior of slender-flange beams is properly represented.

This thesis investigates the true response of flexural members through parametric finite element analysis studies and proposes methodologies to predict the resistances. The proposed methodologies include calculations to account for the post-buckling strength of slender flanges in flexural compression. An effort is made to address local-global buckling interaction effects, where significant, via a modification of the global LTB resistance calculations. The AISC (2016) Specification procedure and the proposed methodologies are compared against the test simulation results and recommendations are provided pertaining to the simplicity of their application and the efficacy of their predictions.

Through a better understanding of flange post-buckling strength and local-global interaction, this research aims to contribute towards the improvement of the Chapter F provisions of AISC Specification.

CHAPTER 1. INTRODUCTION

1.1 AISC (2016) Specification Flexural Strength Limit States

Chapter F of the AISC (2016) Specification provides requirements for the design of steel I-section beams. The Specification implements three independent strength limit state checks – Flange Local Buckling (FLB), Lateral Torsional Buckling (LTB) and Tension Flange Yielding (TFY) – the minimum of which governs the strength of a member. The maximum cross section capacity that can be developed as a function of the web slenderness may be referred to as the plateau resistance, M_{max}. For compact-web members, the plateau resistance for the FLB and LTB limit states is defined as the plastic moment capacity, M_p. For members with webs in the noncompact range, the plateau strength for the FLB and LTB limit states is defined by the web plastification factor, R_{pc}, times the yield moment to the compression flange, M_{yc}. R_{pc} serves as an effective shape factor, equal to M_p/M_{yc} for compact-web sections and is smaller than M_p/M_{yc} for noncompact-web sections. For members with slender webs, the plateau resistance for the FLB and LTB limit states is defined by the web bend-buckling factor, R_{pg}, times M_{yc}. Members are able to develop their plateau strength, $M_{\max}$, in uniform bending if they have compact flanges (defined by $\lambda_f = b_{fc}/2t_{fc} \leq \lambda_{\text{pf}}$) and compact unbraced lengths (defined by $KL_b \leq L_p$). The capacity is reduced for members with noncompact and slender flanges or unbraced lengths in accordance with the AISC FLB and LTB strength curves. Figure 1 (White and Jung, 2008) shows the two strength curves on one plot since their form is the same.

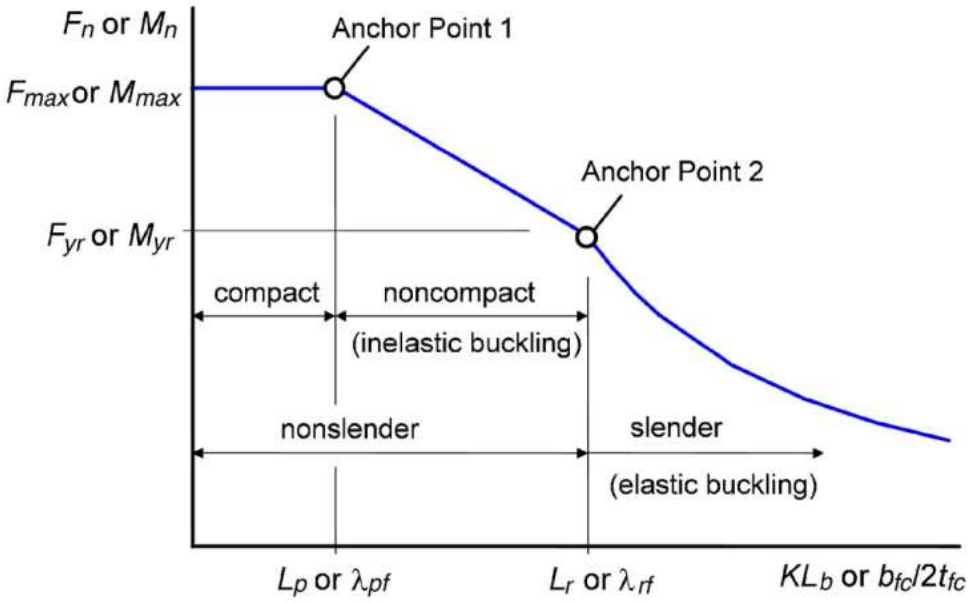

Figure 1: General form of AISC (2016) Specification's FLB and LTB strength curves for member unbraced lengths subjected to uniform bending (White and Jung, 2008)

Figure 1 identifies two "anchor points" pertaining to the FLB and LTB resistances. The first anchor point is tied to $M_{\max}$ and represents the end of the compact region corresponding to L_p on the LTB curve and λ_{pf} on the FLB strength curve. The second anchor point is tied to a compression flange stress value of $0.7F_{yc}$ (in most cases), which represents an idealized first onset of yield in the section. That is, this is the maximum stress at which the member resistance is defined by theoretical elastic FLB or LTB formulas. In terms of moment capacity, this is represented (in most cases) as $0.7M_{yc} = 0.7F_{yc}S_{xc}$. This point corresponds to the noncompact limit, λ_{rf}, on the FLB curve and the noncompact unbraced length limit, L_r, on the LTB curve. Beyond this point, the member strength is idealized as the theoretical elastic FLB or LTB strength.

The TFY limit state checks enter into the calculations only for singly-symmetric members with a compression flange larger than the tension flange. For slender-web members with this characteristic, the TFY check limits the nominal section capacity to the nominal first yield moment to the smaller tension flange, i.e., $M_{yt} = F_{yt} S_{xt}$. For noncompact and compact-web members, the TFY resistance is defined by the web plastification factor R_{pt}, times the yield moment to the tension flange, M_{yt}, recognizing an ability to develop some distributed yielding in tension. The factor R_{pt} is equal to M_p/M_{yt} for a compact-web section.

1.2 Post-buckling FLB Strength and Local-Global Buckling Interaction in I-Section Members

The FLB strength of slender-flange beams (i.e., beams with ($\lambda_f = b_{fc}/2t_{fc}$) $\leq \lambda_{pf}$) is idealized as the theoretical elastic plate local buckling strength in the AISC (2016) Specification. This handling of slender flange members fails to recognize the flange post-buckling reserve strength and tends to give very conservative predictions as the flange becomes more slender. This conservatism is evident from experimental tests documented by White and Jung (2008) and White and Kim (2008). These include tests by Johnson (1985), Holtz and Kulak (1973, 1975), Lew and Toprac (1968), Carskaddan (1968) and Basler et al. (1960). In addition, analytical studies by Seif (2010), Seif and Schafer (2010), Toğay and White (2018) and Toğay (2018) reveal the presence of a significant post-buckling capacity of slender flanges in flexure. In view of these findings, a more refined

strength characterization is desirable for slender-flange members to recognize their post-buckling strength, leading to increased design economy.

In the AASHTO (2017) Specifications, the flange slenderness values are limited to a maximum $b_f/2t_f$ of 12. This is done to guard against flange welding distortion and ensure robustness of rectangular flange plates during fabrication and construction. This restriction essentially disallows the use of slender flange members in the AASHTO (2017) Specifications for yield strengths as high as close to 100 ksi; however, the AISC (2016) Specification does not place any limit on the flange slenderness values. A practical limit of $b_f/2t_f$ = 18 is recommended in AISC Design Guide 25 (White and Jeong, 2020). One application of slender flanges is in metal building design where it is common to use constant-width flanges while stepping the flange thicknesses, tapering the web depths and/or stepping the web thicknesses to achieve design economy. In these types of structures, slender compression flanges may provide the most economical design in areas of low bending moment demand. Moreover, as the use of higher strength steels becomes more common, a greater number of cases will classify as having slender flanges since the λ_{rf} limit becomes smaller. These aspects of design practice provide an impetus for development of a more accurate FLB strength characterization.

Recent research (Toğay and White, 2018) has employed a form of the unified effective width approach (Peköz 1986) to recognize the post-buckling strength of slender flanges in flexure. They showed a notable increase in flexural capacity compared to the theoretical elastic strength prediction by the AISC (2016) Specification, for Grade 55 steel I-section members with flange slenderness values up to $b_f/2t_f$ = 18. This thesis evaluates the approach

suggested by Toğay and White (2018) as well as other similar approaches to characterize the local buckling strength of slender flanges.

While the influence of flange post-buckling resistance has been evident in prior experimental and analytical studies, there is a dearth of research on potential interaction between local and global buckling strengths of I-section beams in flexure. Cherry (1960) conducted experiments evaluating the effect of premature local buckling of thin flanges on the global stability of I-section beams. These tests indicated a significant potential for local-global interaction. More recently, Toğay (2018) and Gerard (2020) have conducted analytical studies evaluating this interaction. While Toğay's research suggests no local-global interaction, Gerard's studies suggest presence of a significant interaction. However, both of these studies had a broader scope and were not targeted to investigate this effect in particular. Therefore, it is not possible to draw clear conclusions regarding potential local-global buckling interaction from these studies. With the scarcity of existing research on this topic, it is clear that additional data is needed to quantify compression flange local post-buckling resistance and potential local-global buckling interaction and inform how these attributes should be addressed in design specification provisions.

1.3 History of the Unified Effective Width Method

The unified effective width method (Peköz, 1986) provides a way of considering the post-buckling strength of slender plate elements as well as local-global buckling interaction. A form of this method is employed in Chapter E7 of the AISC (2016) Specification for the strength calculation of slender-element columns. The method

recognizes that slender plate elements are not able to develop full yielding on their gross cross-section at ultimate load. These elements undergo local buckling resulting in a loss of stiffness and redistribution of stresses.

von Karman et al. (1932) proposed an effective width method to address the reduction in capacity due to local buckling at the ultimate strength of a rectangular plate under axial compression, simply supported on all four edges. According to von Karman et al., this type of plate can be idealized as developing its yield stress over an effective width equal to $b_e/2$ along each of its longitudinal edges and the central portion can be idealized as having zero stress at the ultimate strength condition. This idealization of the actual redistribution of stresses in a slender plate under axial compression is shown in Figure 2.

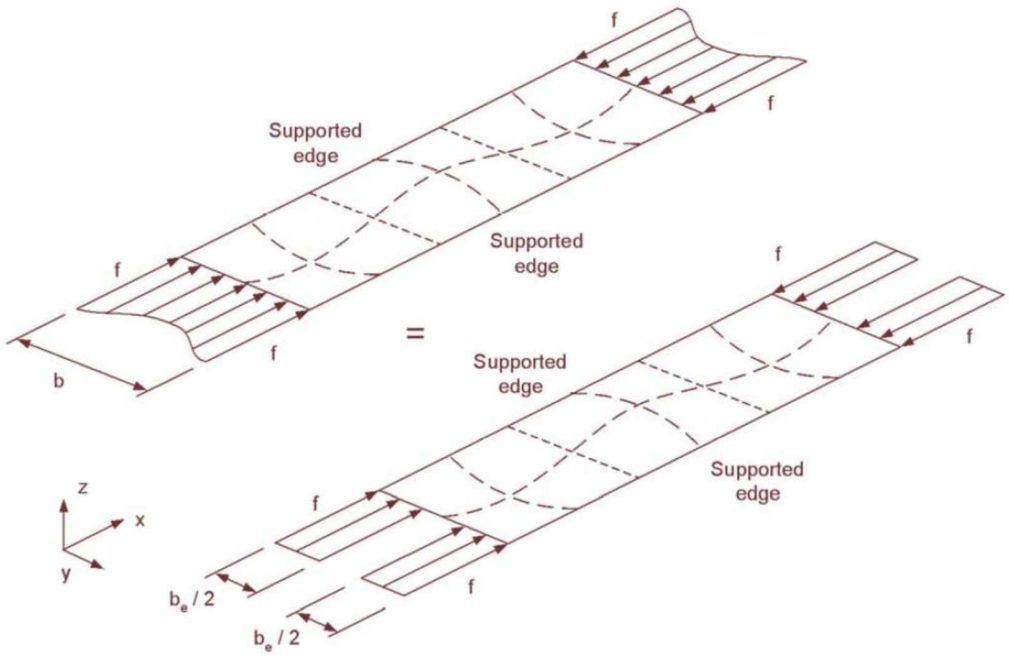

Figure 2: Illustration of average compressive stress distribution across the width of a post-buckled simply supported plate versus idealized equivalent stress distribution acting on the plate effective width (White and Lokhande, 2017)

The effective width equation proposed by von Karman et al. (1932) was followed by many other developments over the years, prior to the adoption of a form of the unified effective width method in the AISC (2016) Specification for columns with slender elements. Winter (1947) recognized that von Karman's equation neglected the presence of small imperfections that amplify under axial load, leading to a load-lateral deflection response of the plate instead of a theoretical response idealized by von Karman et al. Backed by experimental investigations, Winter (1947) developed an empirical modification of the von Karman's effective width equation. Additional testing by Winter (1970) lead to further modification of his recommendations. Equation 1 shows a generalized form of Winter's equation for plates with any edge conditions:

$$b_e = \min\left[b_{fc}\left(1 - 0.22\sqrt{\frac{F_{el}}{F_{yc}}}\right)\sqrt{\frac{F_{el}}{F_{yc}}}, b_{fc} \right] \tag{1}$$

In this equation,

$$F_{el} = \frac{\pi^2 E k_c}{12\left(1-\nu^2\right)\lambda_f{}^2} = \frac{0.9 E k_c}{\lambda_f{}^2} \tag{2}$$

is the theoretical flange elastic buckling stress, where k_c is the flange local buckling coefficient and λ_f is the flange slenderness ratio, defined as $b_f/2t_f$ for I-section flanges.

Equation 1 defines the plate effective width at ultimate load conditions. This is reflected by the use of F_{yc} in Equation 1. Winter found empirically that the same effective width equation can be used to quantify the cross-section stiffness at a given applied stress, f.

DeWolf, Peköz and Winter (1973, 1974) and Kalyanaraman, Peköz and Winter (1972) showed that the overall buckling load can then be calculated using the effective section properties obtained for a given overall buckling stress, F_{cr}. Strictly speaking, this results in an iterative procedure since the buckling stress depends on the effective section properties which in turn depend on the buckling stress. Peköz (1986) proposed the unfied effective width approach, where the effective section properties are calculated using a buckling stress based on the gross section properties. The nominal strength of the member is then found by multiplying this stress by the effective section properties. The unified effective width approach is based on the behavior that the effective width reductions influence the effective area and other effective section properties, such as the effective moment of inertia, in a similar manner such that the impact of the effective width reductions on the critical stress, F_{cr}, is small. For instance, in columns that fail by flexural buckling, if the influence of the effective width reductions is the same for both the area and the moment of inertia, the radius of gyration of the effective cross section is unchanged from that of the gross cross section.

The unified effective width method (Peköz, 1986) was adopted as the basis for the AISI Cold-Formed Steel Specification (AISI, 1986). A form of this procedure has been adopted in AISC (2016) Specification for columns with slender elements. The effective width Equation 1 inherently is employed to consider the post-buckling strength of all the cross-section plate elements. A detailed summary of the development of this procedure is provided in White and Lokhande (2017) and in Ziemian (2010).

It is relevant to state that the Direct Strength Method (the DSM), which was adopted by the North American Specification for the Design of Cold-Formed Steel Structural Members (AISI, 2004) as an alternative to the use of the traditional unified effective width method. The DSM does not involve the calculation of effective widths and directly accounts for local-global buckling interaction in the strength prediction equations. This method is advantageous in that, conceptually, it can be applied to any general cross-section shape. However, since the AISC Specifications have not adopted the DSM, this approach is not investigated in this thesis.

The proposed procedures outlined in Chapter 2 use the unified effective width method to account for post-buckling strength of slender elements and local-global buckling interaction.

1.4 Research Objective

Prior to the adoption of a procedure recognizing post-buckling strength of slender flange members under flexure effects in a future AISC Specification, it is important to investigate any potential local and global buckling interaction in these members. This is currently not addressed in AISC (2016) Specification. It is assumed implicitly that the FLB predictions for slender flanges are already conservative, i.e., the section strength is cut off before any potential local-global interaction is expected to occur. The main focus of this research is to study the presence of the flange local post-buckling strength and any potential local-global buckling interaction using finite element analysis simulations in ABAQUS,

and to investigate alternate methodologies based on the unified effective width approach to characterize these effects, in the context of the AISC (2016) Specification.

This research proposes two methodologies that incorporate the effect of slender flange post-buckling strength as well as considerations for local-global buckling interaction as potential modifications to the AISC (2016) Specification. These new methodologies are presented in Chapter 2 of this document. Chapter 3 discusses the test cases selected for the analytical study and Chapter 4 outlines the finite element analysis procedure. Finally, Chapter 5 presents the test simulation results and provides comparisons with the proposed methodologies as well as the AISC (2016) Specification provisions. The suitability of the proposed methodologies and AISC (2016) provisions are discussed and recommendations for potential development of future AISC Specifications are presented in Chapter 6.

CHAPTER 2. RECOMMENDED METHODOLOGIES

In this chapter, methodologies for flexural strength calculations of welded I-section beams are presented considering slender-flange post-buckling resistance and local-global buckling interaction as an alternate to the AISC (2016) Specification's Chapter F provisions.

The results from the two proposed methodologies and the AISC (2016) Specification are compared with finite element analysis (FEA) test simulations results in Chapter 5. These methodologies are as follows:

1. A procedure considering slender-flange post-buckling FLB strength with no local-global buckling interaction. This will be referred as "FPB-NLG" for brevity, wherein "FPB" refers to "Flange post-buckling strength" and "NLG" stands for "No local-global buckling interaction."
2. A procedure considering slender-flange post-buckling FLB strength as well as local-global buckling interaction. This will be referred as "FPB-LG" for brevity, wherein "FPB" refers to "Flange post-buckling strength" and "LG" stands for "Local-global buckling interaction" considerations.
3. AISC (2016) Specification. These provisions consider neither the slender flange post-buckling FLB strength nor any local-global buckling interaction.

Flowcharts outlining the FPB-NLG, FPB-LG and AISC (2016) Specification procedures are presented in Sections A.1, A.2 and A.3 of Appendix A, respectively.

Moreover, flexural strength calculations for a representative I-section beam in accordance with all three procedures are provided in Appendix B.

In addition to these procedures, an alternate procedure labeled "FPB-NLG-II" is presented in Appendix C. This procedure is based on the same principles as FPB-NLG outlined above but bases the effective width equation on the yield stress of the compression flange, F_{yc}, instead of the overall buckling stress used in FPB-NLG. This eliminates the consideration of the global buckling response on the reductions in the flange effective widths.

Based on recent research, there are a number of key recommendations for improved handling of variables and features in the AISC (2016) Specification. These recommendations are incorporated into the FPB-NLG and FPB-LG procedures. These recommendations are highlighted below before subsequently outlining the above three methodologies in detail.

- Characterization of Tension Flange Yielding (TFY) limit

For sections where the onset of yield occurs at the tension flange before the compression flange, the AISC (2016) Specification imposes a TFY strength limit state. These sections include homogenous singly-symmetric sections having larger flanges in compression (i.e., $S_{xc} > S_{xt}$) or hybrid sections (i.e., sections with different yield strengths of the different plates) having characteristics such that the tension flange experiences yield before the compression flange. For slender-web sections with these characteristics, this limit is taken simply as the yield moment to the tension flange, M_{yt}. Recent research by

Subramanian and White (2017) and Toğay (2018) has shown that this leads to highly conservative designs for such sections. For slender-web sections, the current AISC approach assumes a linear elastic stress distribution through the beam cross-section depth and limits the maximum section capacity to the nominal first yielding of the tension flange. This approach fails to recognize any reserve strength due to the spread of yielding in tension, and leads to an under-utilization of the available section capacity. Toğay (2018) recommends an alternate approach that uses the *true* yield moment to the compression flange, M_{yc}, taking into account the early yielding of the tension flange and the spread of yielding in the tension zone below the neutral axis. A representative stress distribution for these types of cross-sections, determined at the true yield moment of the compression flange, is illustrated in Figure 3.

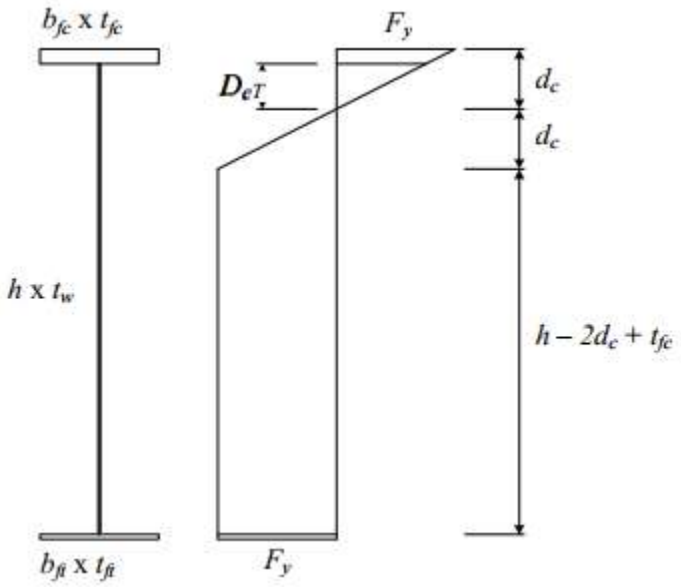

Figure 3: Representative flexural stress profile for the calculation of the true M_{yc} in sections with $S_{xc} > S_{xt}$, considering early yielding of the smaller tension flange and the spread of yielding in the web (Toğay, 2018)

The calculation of the *true* M_{yc} is based on basic principles of mechanics. Toğay and White (2018) provide closed form equations for the *true* M_{yc} calculation for homogenous I-sections. For hybrid sections (i.e., sections with different yield strengths of the different plates), a strain-compatibility analysis can be applied to calculate the true yield moment to the compression flange. The FLB and LTB calculations can then use the *true* M_{yc} of the section, effectively ruling out the need for implementing a TFY strength limit state.

The FPB-NLG and FPB-LG procedures recommended in this research eliminate the use of the TFY limit state by incorporating the use of the *true* M_{yc} into the strength calculations. This is reflected in the flowcharts outlining the procedures in Appendix A. However, for the purpose of this research, only doubly symmetric homogeneous sections are studied. Therefore, the TFY limit does not govern for any case. This means that the calculation of M_{yc} is effectively the same as in the AISC (2016) Specification, i.e., $M_{yc} = F_{yc} S_{xc}$ for doubly symmetric sections.

- Characterization of the LTB limit state

Consistent with the recommendations proposed in Subramanian et al (2018), modifications in the following parameters allow for an improved capture of the actual flexural response of members in light of recent experimental data and advanced test simulation results. These modified parameters are employed in the two proposed procedures, FPB-NLG and FPB-LG, in this study:

i. The compact unbraced length limit, L_p, is taken as $0.63 r_t \sqrt{E / F_y}$. This limit is recommended for cases having negligible warping and flange lateral bending

restraint at the ends of unbraced length, and for cases where end restraint effects are directly accounted for in analysis. A coefficient on 0.8, rather than 0.63, is recommended for "routine" design where some end restraint exists from end connections and or continuity with adjacent unbraced lengths, but these restraint effects are not considered explicitly. For the purpose of this study, the member ends are modeled with multi-point constraints (MPC) that allow for direct application of moments at the ends of the unbraced length while also allowing free warping and flange lateral bending at the ends in the FEA model. Therefore, this recommended value of L_p is used in LTB calculations. More details on the MPC are provided in Chapter 3.

ii. The maximum moment level beyond which characterization by theoretical elastic LTB is no longer sufficient due to residual stresses, geometric imperfections and second-order effects is taken as $0.5M_{yc}$ rather than the typical value of $0.7F_yS_{xc}$ used in AISC (2016) Specification.

- Characterization of the noncompact-web slenderness limit (λ_{rw})

The λ_{rw} limit is taken as follows based on the recommendations by Subramanian and White (2017).

$$\lambda_{rw} = c_{rw}\sqrt{\frac{E}{F_{yc}}} \tag{3}$$

where

$$c_{rw} = \max\left(\min\left(5.7,\ 3.1 + \frac{5}{a_w} \right), 4.6 \right) \tag{4}$$

Based on observations from experimental data and test simulation results, Subramanian and White (2017) observed that members with noncompact webs near the AISC (2016) noncompact web limit tend to behave as slender-web members if their flanges are relatively small compared to the web area. The recommended λ_{rw} captures this effect via the c_{rw} factor.

It is noted again that the above modifications are used in both of the proposed procedures considered in these studies, FPB-NLG and FPB-LG (and in the FPB-NLG-II procedure discussed in Appendix C).

The details of the proposed procedures are explained in the following sections.

2.1 Proposed Procedure I: FPB-NLG (Flange Post-buckling FLB with no Local-Global Buckling Interaction)

The essence of this procedure can be summarized as follows:

i. The flange post-buckling strength of slender flanges in flexural compression is captured in the FLB limit state.

ii. The lateral torsional buckling (LTB) strength calculations are based on gross section properties. As such, these calculations do not account for any local-global interaction. In other words, this assumes that the global LTB strength is not being impacted by the post-buckling deformations of the slender flange.

Toğay and White (2018) capture the slender flange post-buckling strength through an implementation of the unified effective width approach. However, this procedure is slightly modified to simplify the handling of strength in the noncompact flange range. For the welded I-sections being studied, the two proposed procedures utilize the suggested noncompact-slender flange limit of $\lambda_{rf.new} = 0.64\sqrt{\frac{k_c E}{F_y}}$ from Schafer et al. (2020), instead of AISC (2016) Specification's $\lambda_{rf.AISC} = 0.95\sqrt{\frac{k_c E}{F_L}}$ (with F_L taken equal to $0.7F_y$ for doubly symmetric sections). The current $\lambda_{rf.AISC}$ is tied to the $0.7M_{yc}$ anchor point on AISC's theoretical elastic FLB strength curve (Figure 4). Conversely, the suggested $\lambda_{rf.new}$ is tied to a point on the FLB curve where the effective width of the compression flange becomes fully developed as per the unified effective width equation (Winter, 1970) i.e., $M_n = M_{yc}$ at $\lambda_f = \lambda_{rf.new}$. This distinction in the handling of the anchor point at λ_{rf} in AISC and the proposed procedures (FPB-NLG and FPB-LG) is illustrated in Figure 4 below. Beyond $\lambda_{rf.new}$, the proposed procedures utilize the unified effective width approach to characterize the strength of slender flange members in flexural compression.

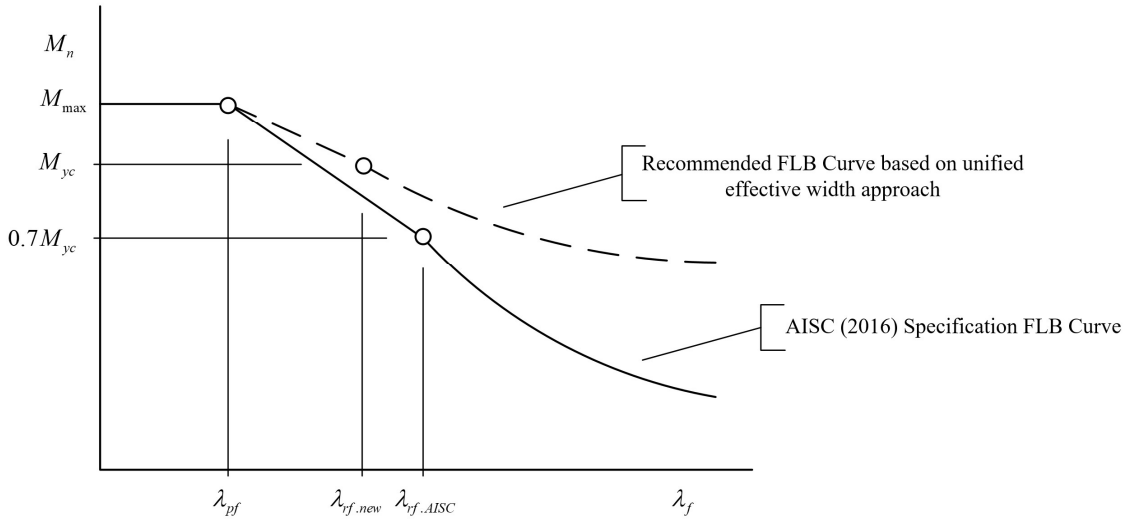

Figure 4: Representation of a comparison between AISC (2016) Specification's FLB curve and the recommended FLB curve based on unified effective width approach accounting for flange post-buckling strength in the slender region

The calculation of the section resistance for slender flange sections, for which $\lambda_f \geq \left[\lambda_{rf.new} = 0.64\sqrt{\frac{k_c E}{F_y}} \right]$, is conducted as follows.

a) The effective width of the slender flange in flexural compression is based on the overall buckling stress defined as $F_{ngLTB} = M_{ngLTB}/S_{xc} \leq F_y$ following the principles of the unified effective width procedure (Peköz, 1986). Here M_{ngLTB} is the member global (LTB) strength based on gross section properties. The effective width equation is therefore

$$b_e = \min\left[b_{fc}\left(1 - 0.22\sqrt{\frac{F_{el}}{F_{ngLTB}}}\right)\sqrt{\frac{F_{el}}{F_{ngLTB}}}, b_{fc} \right] \quad (5)$$

where, the flange elastic buckling stress is given by:

$$F_{el} = \frac{0.9Ek_c}{\lambda_f^{\,2}} \tag{6}$$

b) Given the effective width, b_e, the effective section parameters are calculated. These include the location of the neutral axis relative to the inside of the compression flange, D_{ce}, the effective section moment of inertia, I_{xce}, and the effective section modulus, S_{xce}.

c) An effective web bend buckling strength reduction factor for slender webs, R_{pge}, is computed using the effective section properties. For effective sections with noncompact and compact webs, $R_{pge} = 1$.

d) In general, these parameters are used to compute the *true* M_{yce} accounting for early yielding in tension flange for $S_{xt} < S_{xce}$. For the purpose of this study, all tests sections are doubly symmetric, therefore, $M_{yce} = F_y S_{xce}$.

e) The resistance corresponding to a slender flange section is then calculated as $M_{n(FLB)} = R_{pge} M_{yce}$.

For flanges in the noncompact range ($\lambda_{pf} < \lambda_f < \left[\lambda_{rf.new} = 0.64\sqrt{\frac{k_c E}{F_y}} \right]$), the strength of the section is calculated as a simple interpolation between the first anchor point (λ_{pf}, $M_{.max}$) and the second anchor point ($\lambda_{rf.new}$, $R_{pg}M_{yc}$) on the recommended FLB curve shown in Figure 4. Here M_{max} is the plateau resistance for the FLB curve corresponding to the plastic moment M_p for compact-web sections, $R_{pc}M_{yc}$ for noncompact-web sections and $R_{pg}M_{yc}$ for slender-web sections. The formula for this interpolation is

$$M_{n(FLB)} = R_{pg} M_{yc} \left[R_{pc} - \left(R_{pc} - 1 \right) \left(\frac{\lambda_{fc} - \lambda_{pf}}{\lambda_{rf} - \lambda_{pf}} \right) \right] \tag{7}$$

where R_{pg} = 1.0 for compact- and noncompact-web sections and R_{pc} = 1.0 for slender-web sections.

One aspect of this approach for calculating the FLB resistance is that slender-web sections do not have any noncompact flange range. This is because λ_{pf} and $\lambda_{rf.new}$ for these sections are equal to one another. Slender-web sections are restricted to a plateau resistance of $R_{pg}M_{yc}$ on the FLB strength curve. The end of plateau resistance is marked by $\lambda_f = \lambda_{pf}$. This point also is the location where the full width of the flange becomes fully developed signifying the beginning of Winter's curve ($b_e = b$). It thereby also acts as the location of the second anchor point $\lambda_{rf.new}$ corresponding to $R_{pg}M_{yc}$.

The FPB-NLG procedure uses the gross section properties for the calculation of the LTB resistance, M_{ngLTB}. That is, this procedure does not recognize any reduction in LTB resistance due to any early onset of local buckling of the slender compression flange. In other words, it assumes that no local-global buckling interaction occurs (in the sense that the flange effective widths are not considered in determining the global LTB capacity).

The FPB-NLG procedure and relevant equations are summarized in a flowchart form in Section A.1 of Appendix A.

It is noted that the alternate "FPB-NLG-II" procedure outlined in Appendix C is based on the same principles as the FPB-NLG procedure but uses the yield stress of the

compression flange, F_{yc}, in the effective width equation instead of the overall buckling stress defined as $F_{ngLTB} = M_{ngLTB}/S_{xc} \leq F_{yc}$.

It can be stated that the above FPB-NLG procedure actually involves local-global interaction in that the global buckling stress is utilized in the calculation of the compression flange local buckling resistance. However, the FPB-NLG procedure does not consider any influence of the compression flange effective width reductions on the global lateral-torsional buckling resistance. By employing F_y in the calculation of the compression flange effective width in the FPB-NLG-II procedure, there is also no effect of the global lateral-torsional buckling response on the flange local buckling strength.

2.2 Proposed Procedure II: FPB-LG (Post-buckling FLB with Local-Global Buckling Interaction)

The essence of this procedure can be summarized in the following points:

i. The flange post-buckling strength of slender flanges in compression is captured in the FLB limit state. This is done the same way as in FPB-NLG procedure.

ii. The lateral torsional buckling (LTB) strength calculations are modified using the unified effective width approach to account for loss in section global capacity resulting from local buckling. That is, an effort is made to characterize and account for local-global buckling interaction.

The FLB post-buckling strength calculations provided under FPB-NLG procedure are followed for this procedure as well.

In this approach, the handling of the effective LTB calculations is conducted in a way similar to the treatment of the strength of slender element columns in Section E7 of AISC (2016). This follows the principles of the unified effective width approach recommended by Peköz (1986) where the nominal strength in terms of a stress is found for the gross section and then the nominal resistance is found by multiplying this stress by an effective section modulus. The effective section properties are calculated using the effective width, b_e, calculated using Winters (1970) effective width equation. The FPB-LG procedure calculates a gross-section LTB capacity ($M_{ng.LTB}$) and then scales this by the ratios of M_{yce}/M_{yc} and R_{pge}/R_{pg}.

The procedure and relevant equations are summarized in flowchart form in Section A.2 of Appendix A.

CHAPTER 3. TEST PLAN FOR ANALYTICAL STUDIES

3.1 General Considerations

This research focuses on doubly symmetric beams. All the test members have homogenous material properties and a single unbraced length, braced against out-of-plane lateral deflection and twisting at the member ends.

Illustrations of the load and displacement boundary conditions for uniform moment and moment gradient cases are shown in Figures 5 and 6, respectively.

Figure 5: Test member load and displacement boundary conditions for uniform moment studies

Figure 6: Test member load and displacement boundary conditions for moment gradient studies

Similar to the considerations in Kim (2010), the member ends are modelled with specialized multi-point constraints to replicate the following kinematic end conditions:

a) End rotations within the plane of a member are unrestrained.
b) One vertical support is idealized as a pin while the other is idealized as a roller.
c) Out-of-plane end rotations of the member are unrestrained.
d) The member end cross-section warping displacements are unrestrained (i.e., the member flanges are free to "cross-bend" in opposite directions at member ends).
e) Plane sections are constrained to remain plane individually at the centerline of the web thickness, and separately, at the centerlines of the flange thicknesses at the end cross-sections.

Test plans to evaluate the two main parameters investigated in this study are discussed in the following sections.

3.2 Characterization of the FLB Limit State

The FLB limit state proposed in the FPB-LG and FPB-NLG approaches differs from the AISC (2016) Specification's approach as discussed in Section 2.1 and illustrated in Figure 4. The proposed procedures use the unified effective width approach to characterize the slender flange post-buckling strength. In contrast, AISC (2016) characterizes the slender flange FLB strength as the theoretical elastic plate buckling strength, which ignores the beneficial post-buckling capacity of slender flanges. This leads to highly conservative strength predictions for flanges with higher slenderness. Moreover, the proposed

procedures use a different $\lambda_{rf.new} = 0.64\sqrt{\frac{k_c E}{F_y}}$ recommended by Schafer et al. (2020) instead of the AISC (2016) Specification's $\lambda_{rf.AISC} = 0.95\sqrt{\frac{k_c E}{0.7F_y}}$.

To investigate the adequacy of the proposed procedures versus the AISC (2016) Specification, an FEA test plan is designed to study sections failing by FLB. The unbraced length of these sections is kept constant at (L_b = 25 in) < L_p to ensure plateau strength LTB conditions. The calculated L_p values for the sections studied range from 26.8 to 34.8 inches. The flange thicknesses are varied to study a range of flange slenderness values for compact-web, noncompact-web and slender-web sections. The web depth, h, is held constant at 28 inches for all the sections while the web thickness is varied. Similarly the flange width, b_f, is kept constant at 9 inches while the flange thickness is varied. All the test sections are homogeneous, have a yield strength of 60 ksi and are subjected to uniform moment as illustrated in Figure 5. Table 1 outlines the test members studied in the FEA simulations. The test names are chosen to reflect the web and flange slenderness of the test member. "SW", "NCW" and "CW" denote slender, noncompact and compact webs respectively while the number immediately after is the flange slenderness value $b_f/2t_f$. All these studies are conducted assuming a nominal yield strength of F_y = 60 ksi.

Table 1: Test sections for FEA studies focused on evaluating the flange post-buckling resistance (b_f = 9 inches, h = 28 inches and L_b = 25 inches).

Test Case	Test Name	$b_f / 2t_f$	h / t_w
Slender Web Members	SW-7	7	149.3
	SW-9	9	149.3
	SW-11	11	149.3
	SW-13	13	149.3
	SW-15	15	149.3
	SW-18	18	149.3
Noncompact Web Members	NCW-7	7	93.3
	NCW-9	9	93.3
	NCW-11	11	93.3
	NCW-13	13	93.3
	NCW-15	15	93.3
	NCW-18	18	93.3
Compact Web Members	CW-7	7	70
	CW-9	9	70
	CW-11	11	70
	CW-13	13	70
	CW-15	15	70
	CW-18	18	70

3.3 Investigation of Local-Global Buckling Interaction

The following additional FEA test simulations are designed to evaluate sections and member lengths deemed most susceptible to potential local-global buckling interaction. The targeted test sections can be classified into the following five cases:

i. Case 1: Slender flange – slender web sections under uniform moment loading having F_y = 60 ksi
ii. Case 2: Slender flange – slender web sections under uniform moment loading having F_y = 100 ksi
iii. Case 3: Slender flange – compact web sections under uniform moment loading having F_y = 60 ksi
iv. Case 4: Slender flange – compact web sections under uniform moment loading having F_y = 100 ksi
v. Case 5: Slender flange – slender web sections subject to a linear moment gradient having F_y = 60 ksi

A flange slenderness of $b_f/2t_f$ = 18 is selected for all the test sections in this study. This is the upper limit of allowable flange slenderness recommended by AISC Design Guide 25 (White and Jeong, 2020) and represents the most-slender flange applications expected in practice for welded I-section members. The post-buckling deformations of these flanges is expected to have the most potential impact on the global buckling strength. The slender web sections studied have relatively deep webs compared to the compact web sections, which have relatively shallow webs. The shallower webs are selected to evaluate situations

where the strength of sections may become more dominated by FLB behavior. This is because the elastic properties in these sections, such as moment of inertia, have smaller contributions from the web. A small sample of beams under moment gradient are selected to test the handling of these effects against simulation results.

The section dimensions for the five member types studied in this section are given in Table 2.

The unbraced length of each section type is varied from approximately $L_b = L_p$ to approximately $L_b = L_r$ to investigate the local-global interaction. The notation for the test names is selected to uniquely define each section type. As an example, test member "UM-LB85-SF-SW-60" indicates a doubly symmetric section under uniform moment with an unbraced length of 85 in, slender flanges, a slender web and F_y = 60 ksi. The notations "MG" and "CW" appearing in the member names in Table 2 stand for "Moment Gradient" and "Compact Web" respectively.

Table 2: Test cases for study of potential local-global buckling interaction (b_f = 9 in and $b_f/2t_f$ = 18 in).

Case	Description	Test Name	h / t_w	h
1	Slender Flange – Slender Web, Uniform Moment, F_y = 60 ksi	UM-LB-SF-SW-60	149.3	28
2	Slender Flange – Slender Web, Uniform Moment, F_y = 100 ksi	UM-LB-SF-SW-100	149.3	28
3	Slender Flange – Compact Web, Uniform Moment F_y = 60 ksi	UM-LB-SF-CW-60	36	9
4	Slender Flange – Compact Web, Uniform Moment F_y = 100 ksi	UM-LB-SF-CW-100	36	9
5	Slender Flange – Slender Web, Moment Gradient, F_y = 60 ksi	MG-LB-SF-SW-60	149.3	28

CHAPTER 4. FINITE ELEMENT MODELING

The identified test members are modeled in the ABAQUS 6.13 Standard (Simulia, 2013) finite element analysis software system. The following sections outline the modeling considerations.

4.1 Element Type and Mesh Discretization

The webs and flanges of the members are modeled using the S4R element, which is a four-node quadrilateral large strain shell element formulation. The members are tested in full non-linear finite element analyses, including material and geometric non-linearity. The mesh density corresponds to 12 elements along the flange width and 30 elements along the web depth for 28 inch deep web members. For the 9 inch deep web members studied, 12 elements are employed along web depth. This relatively dense mesh performs well in terms of convergence of the finite element solution and is chosen as a result of a mesh discretization study by Subramanian (2015). The number of elements along the length are calculated such that the aspect ratio of each element is approximately 1.0 within the web. Figures 7 and 8 show finite element models of representative members with 28 inch and 9 inch deep webs respectively.

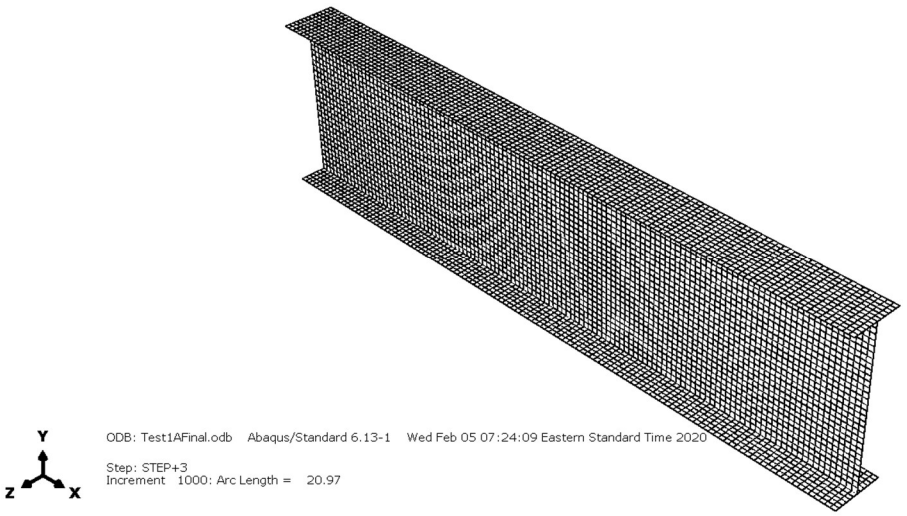

Figure 7: Finite element model of a representative test member with a 28 inch deep web in ABAQUS 6.13

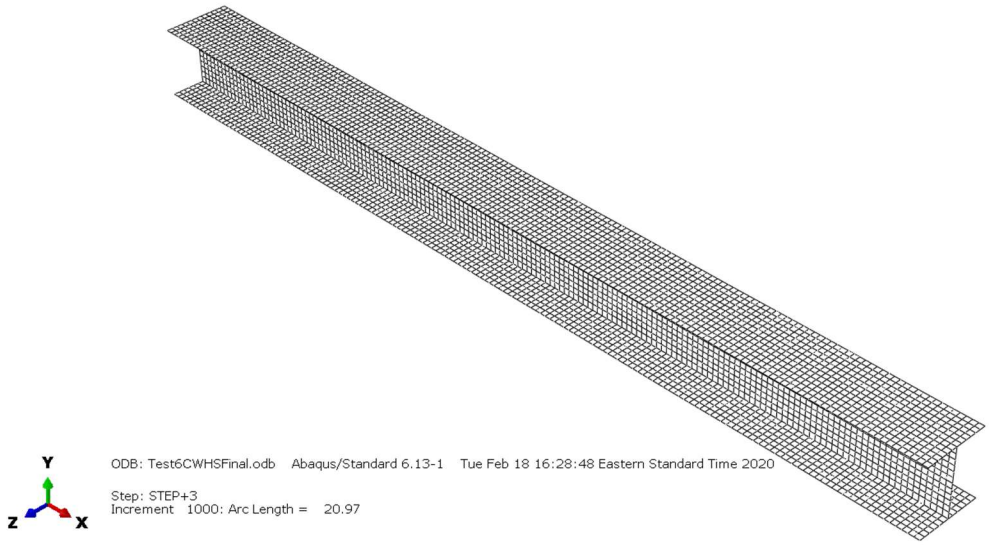

Figure 8: Finite element model of a representative test member with a 9 inch deep web in ABAQUS 6.13

4.2 Material Properties

The test members are modeled using a J2 plasticity model with isotropic hardening which recognizes that during plastic straining the Mises yield stress surface expands as the stress state increases beyond the initial yield condition. All test sections have homogenous material properties corresponding to either F_y = 60 ksi or F_y = 100 ksi depending on the test case being studied. The modulus of elasticity (E) is taken as 29,500 ksi which represents a common mean value for structural steel. For the Grade 60 steels, the post-elastic stress-strain response is modelled with a tangent stiffness of E/1000 up to a strain-hardening strain value of 10 times the yield strain (ε_y). The strain hardening modulus is modeled after this point as E/50. This is a common basic representation of the stress-strain response of ordinary structural steels, and is adequate for the test simulations under consideration since the strain levels observed exceed the strain hardening strain by a minor amount and only within localized regions in these studies (ASCE, 1971). For the Grade 100 steels, a constant post-elastic tangent stiffness of E/1000 is employed without any characterization of strain-hardening. This provides a representation of the stress-strain response for some of these types of steels, such as the plates employed in the girder tests by Fahnestock (1998). Some high-strength steels do not exhibit a sharp yield response. This potential attribute is not addressed in this research.

4.3 Residual Stresses

The "Best-fit Prawel" residual stress pattern used previously by Kim (2010) and Subramanian (2015) has been adopted for these studies. The residual stress values are

halved based on the recommendations by Subramanian and White (2017a, 2017b, 2017c) to provide a more realistic correlation with the mean results from experimental tests. Additionally, the web residual stresses are taken equal to zero. This is a reasonable approximation for the slender web h/t_w values studied, since the slender webs would buckle prior to reaching the web compressive residual stresses defined in the Best-fit Prawel pattern. For the members with the stockiest compact webs, the web can sustain these compressive stresses; however, the residual stresses in the web have a minor impact on the member response in these cases. The residual stress pattern employed for the studies is illustrated in Figure 9.

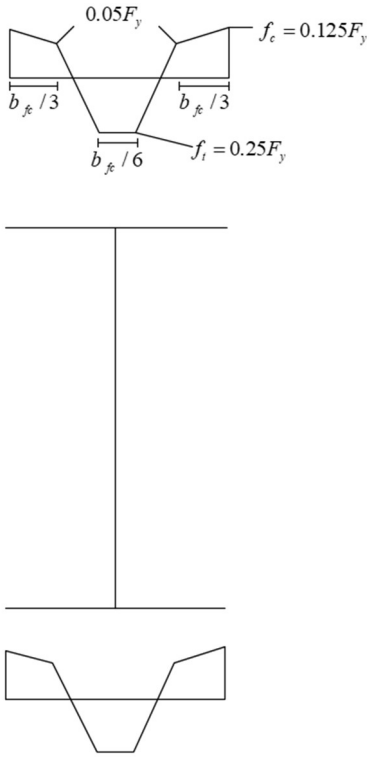

Figure 9: Residual stress pattern employed in test studies corresponding to one-half the values of "Best-fit Prawel" pattern.

4.4 Geometric Imperfections

The idealized geometric imperfection patterns employed in Toğay (2018) are used in this study. Three types of geometric imperfections namely flange tilt, web out of flatness and flange sweep, are considered. The flange tilt and web out-of-flatness patterns are obtained by executing an elastic eigenvalue buckling analysis of the test member subjected uniform axial compressive stress, and in which the web-flange juncture locations are continuously constrained against lateral displacement. Figure 10 shows the resulting scaled deformed shape of a representative test member.

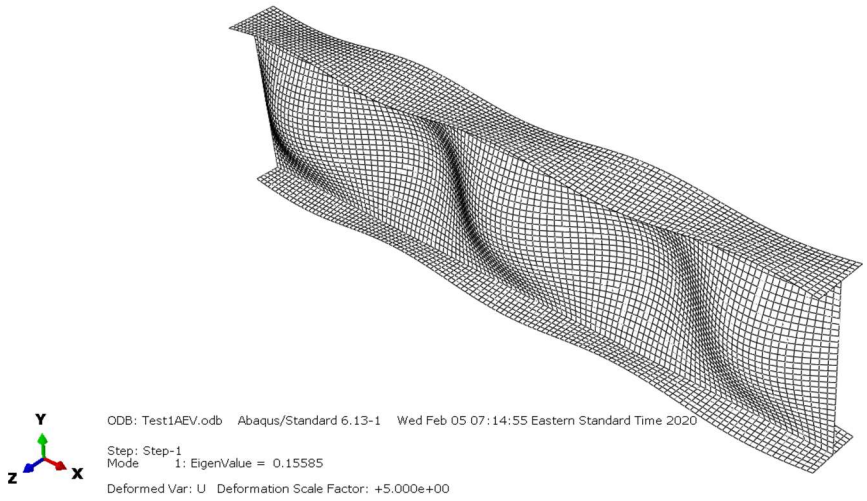

Figure 10: Deformed shape of a test member under uniform axial compression obtained by an elastic eigenvalue buckling analysis (displacement scale factor = 5.0)

The buckling mode obtained is scaled separately for the web and for the flanges to one-half the tolerance values noted in AWS (2010) and the AISC Code of Standard Practice (COSP), as shown in Figure 11. This is done considering the recommendations from

Subramanian and White (2017a), which are intended to provide correlation with the mean results from experimental tests.

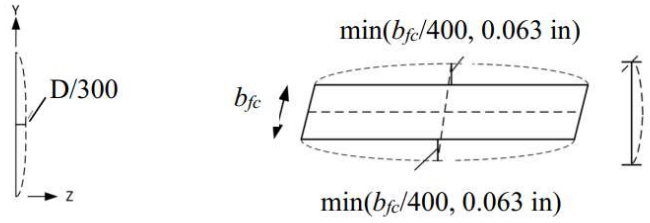

Figure 11: Web out-of-flatness and flange tilt imperfections

A flange sweep corresponding to the pattern shown in Figure 12 is applied at the web-compression flange juncture. The tension flange is held straight when generating this imperfection. The resulting scaled deformed shape for a representative test member having only a flange sweep imperfection is shown in Figure 13.

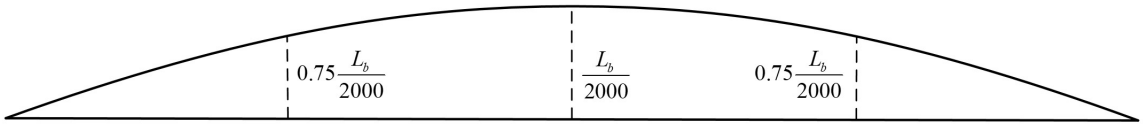

Figure 12: Flange sweep imperfection

A verification and validation study of the FEA procedure is provided in Appendix D.

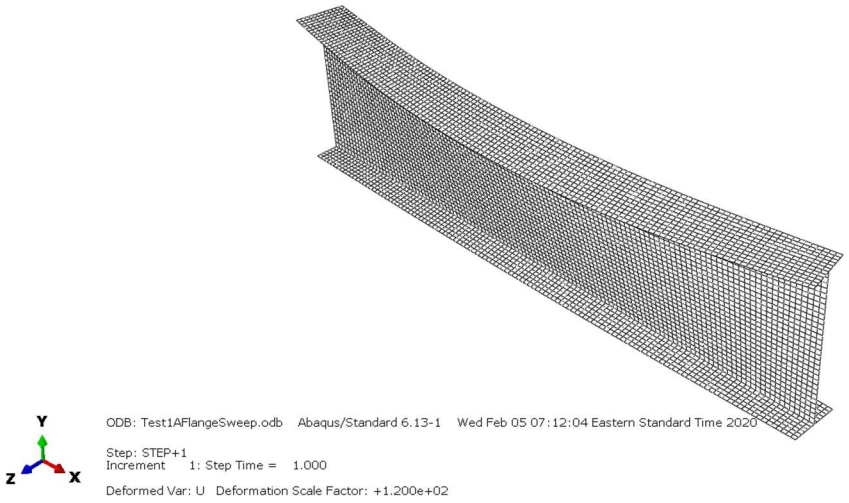

Figure 13: Deformed shape of a test member with flange sweep imperfection only (displacement scale factor = 120.0)

CHAPTER 5. RESULTS AND DISCUSSIONS

This chapter presents the results of the FEA test simulations for the two targeted studies outlined in Chapter 3.

5.1 Characterization of the FLB Limit State

The member tests outlined in Table 1 of Chapter 3 are simulated to evaluate the ultimate strength response. All the members have (L_b = 25) < L_p in to ensure plateau strength LTB conditions. The FPB-NLG, FPB-LG and AISC (2016) procedures predict an FLB failure mode for all these members. This is also reflected in the deformed shapes at the peak load, which are scaled by a factor of 5.0 in Figures 14 through 19. The plastic equivalent strain (PEEQ) contours at the top surface of the shell elements is shown on the rendering of the deformed geometry. The PEEQ contours are useful in identifying regions that have yielded at peak load. The dark blue contours represent locations behaving elastically while the remaining colored contours indicate locations where different magnitudes of yielding have occurred.

All the test members shown in Figures 14 through 19 show predominant yielding of the compression flange at their maximum load capacity. Members with slender webs show the largest flange deformations (see Figures 18 and 19) compared to noncompact-web and compact-web members for a given flange slenderness. In addition, the members with a flange slenderness, $b_f/2t_f$, of 18 expectedly show larger deformations than stockier flanges with $b_f/2t_f$ = 7 at the peak load.

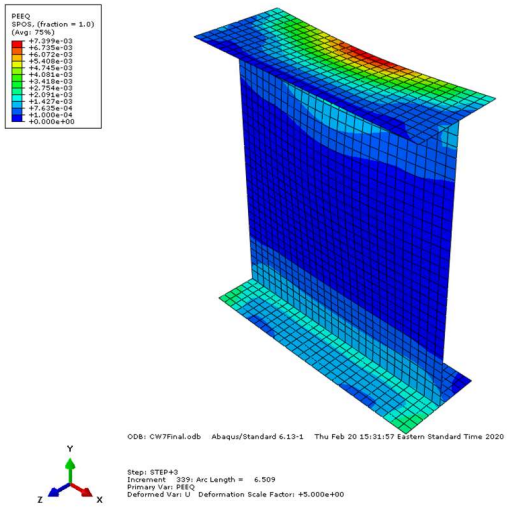

Figure 14: Deformed shape at peak load of a compact-web section with $b_f/2t_f = 7$ plotted with PEEQ (plastic equivalent strain) contours (displacement scale factor = 5.0)

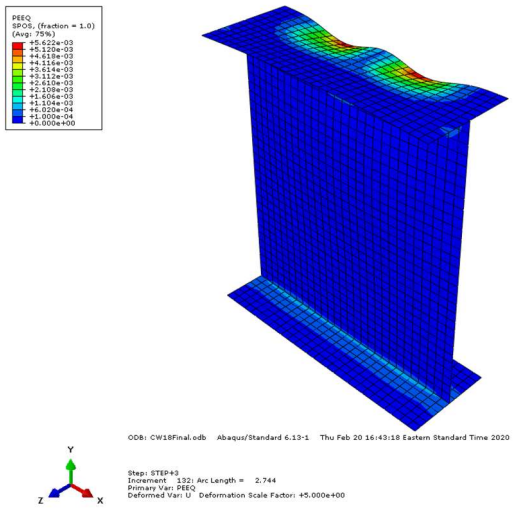

Figure 15: Deformed shape at peak load of a compact-web section with $b_f/2t_f = 18$ plotted with PEEQ (plastic equivalent strain) contours (displacement scale factor = 5.0)

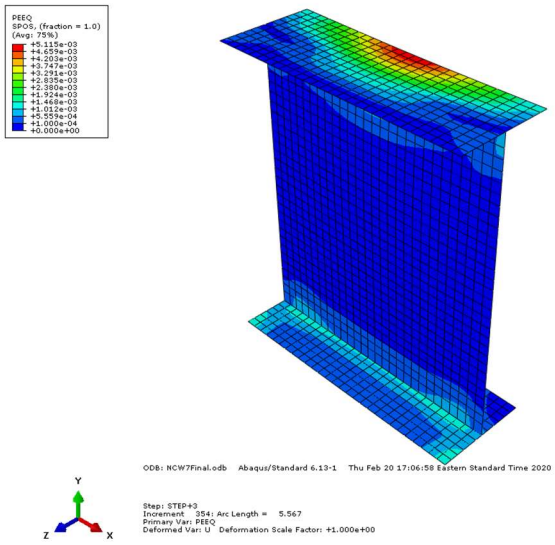

Figure 16: Deformed shape at peak load of a noncompact-web section with $b_f/2t_f = 7$ plotted with PEEQ (plastic equivalent strain) contours (displacement scale factor = 5.0)

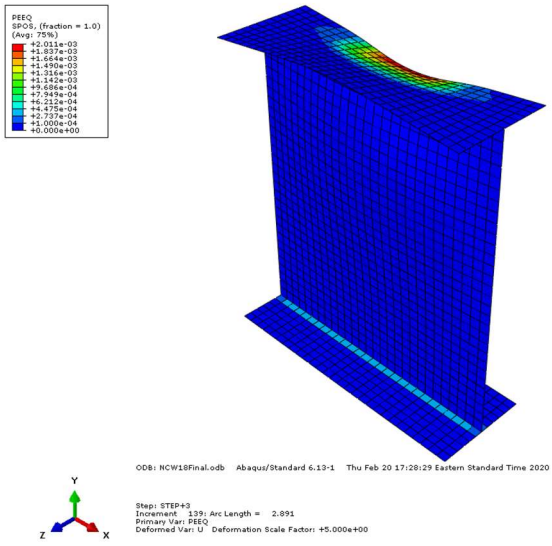

Figure 17: Deformed shape at peak load of a noncompact-web section with $b_f/2t_f = 18$ plotted with PEEQ (plastic equivalent strain) contours (displacement scale factor = 5.0)

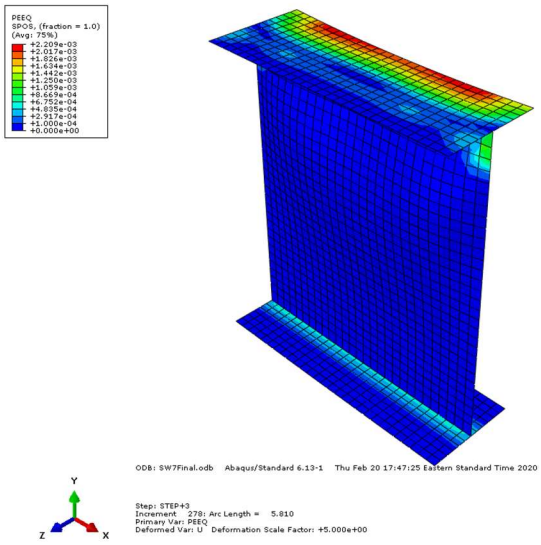

Figure 18: Deformed shape at peak load of a slender-web section with $b_f/2t_f = 7$ plotted with PEEQ (plastic equivalent strain) contours (displacement scale factor = 5.0)

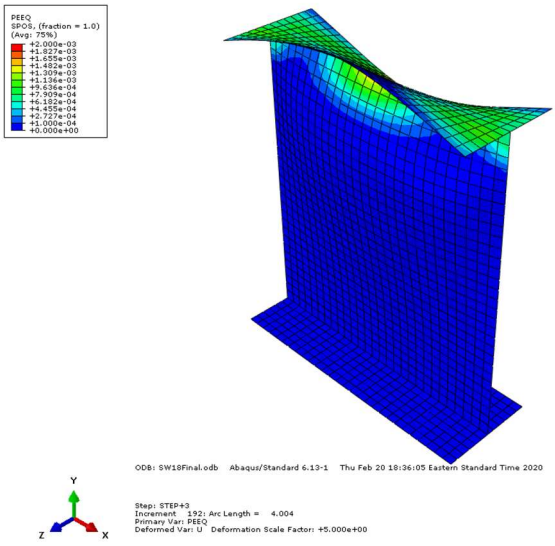

Figure 19: Deformed shape at peak load of a slender-web section with $b_f/2t_f = 18$ plotted with PEEQ (plastic equivalent strain) contours (displacement scale factor = 5.0)

The peak strengths obtained from the FEA analysis for the test members in Table 1 (Chapter 3) are plotted against the strength predictions from the proposed and AISC (2016) Specification procedures in Figures 20 through 22. Since all the tests fail in an FLB mode, the FPB-LG and FPB-NLG predictions are same for all tests and will simply be referred as FPB in the plots. This is because both these procedures propose the same handling of the FLB limit state. Figures 20 through 22 show the results for members with slender webs, noncompact webs and compact webs respectively.

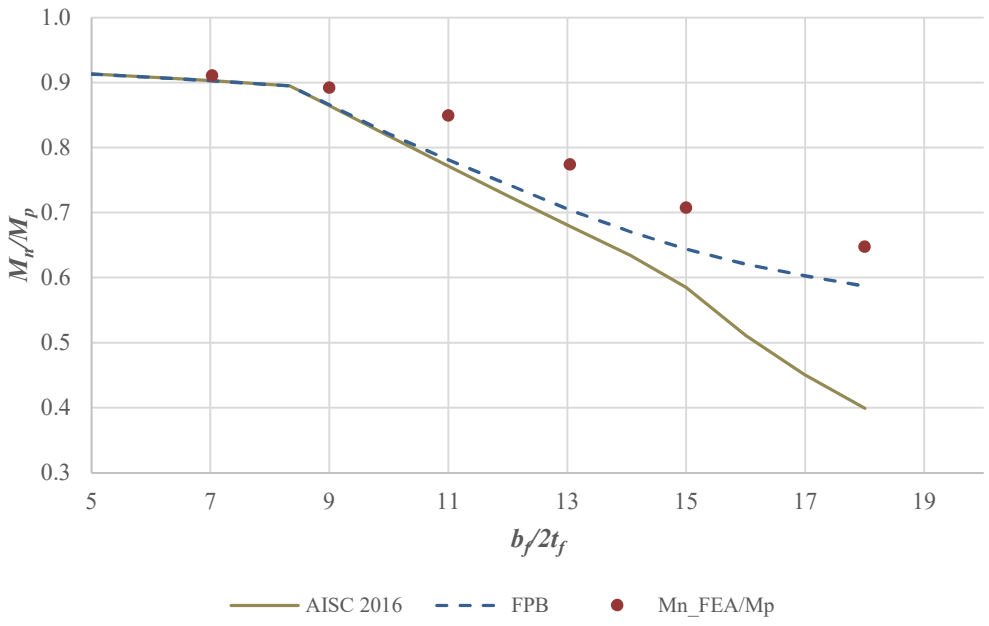

Figure 20: Comparison of strength predictions by FEA simulations, AISC (2016) and FPB procedures with flange slenderness for slender-web members

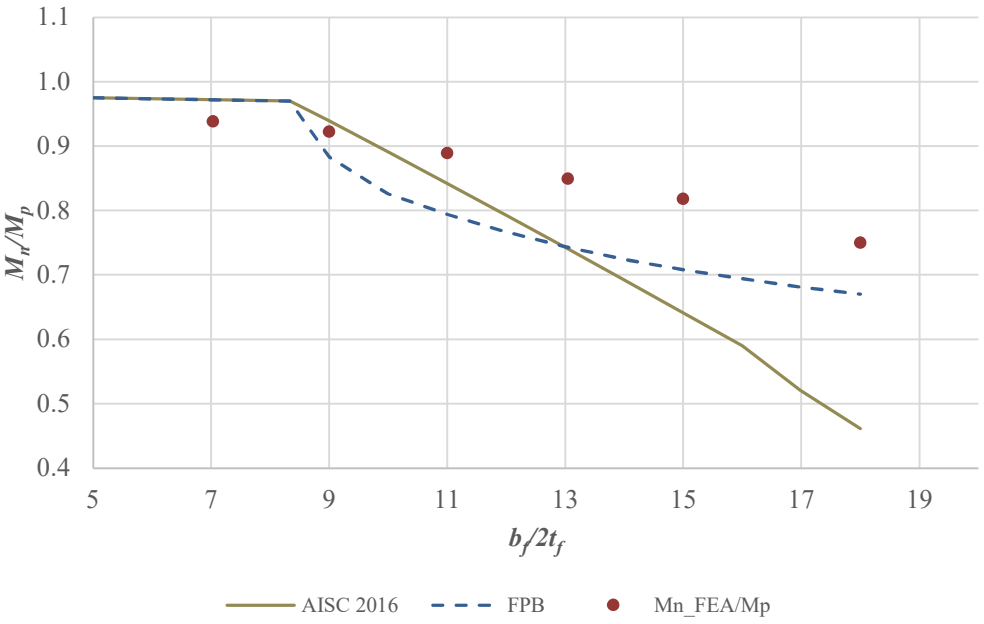

Figure 21: Comparison of strength predictions by FEA simulations, AISC (2016) and FPB procedures with flange slenderness for noncompact-web members

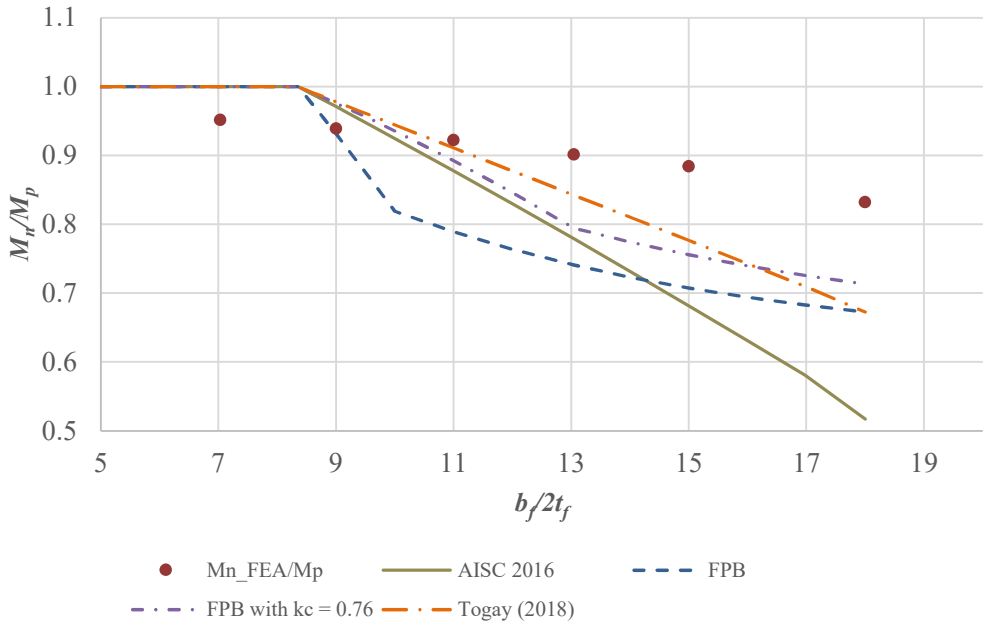

Figure 22: Comparison of strength predictions by FEA simulations, AISC (2016), FPB, "FPB with k_c = 0.76" and Togay (2018) procedures with flange slenderness for compact-web members

The above plots show that the proposed FPB procedure gives a better strength prediction compared to the AISC (2016) procedure for members with highly slender flanges. The AISC (2016) curve diverts from the proposed curve as the flange slenderness increases due to its lack of accounting for the flange post-buckling strength. This leads to highly conservative predictions for slender flanges per AISC (2016). For a slender-web section with $b_f / 2t_f$ of 18 (Figure 20), AISC (2016) shows a 62.2% conservative estimate compared to the FEA prediction while the proposed procedure shows 11.4% conservatism. The AISC strength prediction is therefore 45.5% more conservative than the proposed procedure for this section. For the slender-flange member having $b_f / 2t_f = 18$ and a compact web (Figure 22), the proposed procedure gives a 20.4% conservative estimate while the AISC (2016) prediction is conservative by 61% for the same section. It is noted that the proposed procedure gives the closest approximation of the FEA results for the slender-web sections (Figure 20). As the web gets stockier, the strength predictions by the proposed procedures become more conservative (Figures 21 and 22).

The proposed FPB curves for noncompact-web sections (Figure 21) and compact-web sections (Figure 22) show a steep transition in the noncompact flange range. This leads to conservative predictions for sections with flanges around the noncompact limit compared to AISC (2016). It is noted that this may be due to the simplified characterization of the local plate buckling coefficient, k_c, which influences the calculation of the noncompact flange limit in these procedures, i.e., $\lambda_{rf.new} = 0.64\sqrt{\frac{k_c E}{F_y}}$. This characterization of k_c is adopted from the AISC (2016) Specification which uses the same k_c coefficient for a given

cross-section type regardless of the characteristics of the flange, ignoring the presence of any interaction between the flange and web of the section.

Seif and Schafer (2010) have shown that this coefficient is in fact influenced by the combined web and flange dimensions of the section. A more accurate characterization of k_c would account for the additional restraint provided by thicker webs in Figures 21 and 22, leading to a higher noncompact flange limit. This would result in a shallower noncompact flange transition in Figures 21 and 22 and a closer approximation to the FEA results. Figure 22 illustrates this effect by plotting an additional strength curve noted as "FPB with $k_c = 0.76$", which represents the upper limit value of k_c in AISC (2016). This is done for illustration purposes only. For these compact-web sections (Figure 22), the AISC (2016) value of k_c is 0.478, which is used in all other strength curves in Figure 22. It is evident that the use of a higher k_c of 0.76 increases the noncompact flange limit and gives better correlation with FEA results. It is suggested that an improved characterization of k_c would be an important next step in future studies to ensure proper representation of the flange local buckling limit state for I-section members. Seif and Schafer (2010) recommend equations for an accurate calculation of k_c based on cross-section elastic local buckling studies. Based on the results shown in Figure 22, it appears that a larger effective k_c is needed for improved correlation of the design calculation results with the FEA simulation results. This may be due to the reduction in stiffness of the compression flange due to partial yielding, and the influence this yielding has on the relative rotational restraint provided by the web at the web-to-flange juncture.

The approach to representing the post-buckling FLB strength of slender flanges recommended by Togay (2018) is also plotted on Figure 22. This approach establishes the second anchor point on the FLB curve corresponding to $\lambda_{rf.AISC} = 0.95\sqrt{\frac{k_c E}{0.7F_y}}$ and $M_{yce(\lambda rf.AISC)}$. Here, $M_{yce(\lambda rf.AISC)}$ is the post-buckled strength of the given section at $\lambda_f = \lambda_{rf.AISC}$, given by Winter's curve and computed following the principles of the unified effective width approach. The interpolation between the first anchor point (λ_{pf}, $M_{nFLB.max}$) and the second anchor point ($\lambda_{rf.AISC}$, $M_{yce(\lambda rf.AISC)}$) gives the noncompact flange curve per Togay (2018). This differs from the FPB approach, which establishes the second anchor point at $\lambda_{rf.new} = 0.64\sqrt{\frac{k_c E}{F_y}}$ corresponding to M_{yc}. As shown in Figure 22, Togay's approach also gives some improvement in the correlation with the FEA results. Both the FPB and Togay (2018) curves in Figure 22 converge to Winter's curve for sections having $\lambda_f > \lambda_{rf.AISC}$.

The above discussion for the sections in Figure 22 can be extended to noncompact-web sections having intermediate flange slenderness values in Figure 21 as well, which also shows some conservatism of the FPB approach relative to the FEA test simulation results. In terms of simplicity of the calculations, the FPB approach has an advantage over Togay's approach for noncompact-flange sections since it does not require any effective width calculations for these sections. Conversely, Togay's approach requires the calculation of $M_{yce(\lambda rf.AISC)}$, based on the effective section properties corresponding to $\lambda_{rf.AISC}$, to establish the second anchor point of the noncompact flange curve. However, Togay's approach gives

better correlation with the FEA simulation strengths compared to the FPB approach for the tests considered here. As noted earlier, a more rigorous accounting for the local plate buckling coefficient k_c would lead to better strength predictions by the FPB approach as illustrated in Figure 22. Regardless of the handling of noncompact flanges, both approaches converge to the use of Winter's curve for sections having $\lambda_f > \lambda_{rf,AISC}$. All of these procedures give improved strength predictions compared to AISC (2016) for highly slender flanges.

The plateau resistance of the FLB curves in Figures 20 through 22 is characterized in the same manner in both the AISC (2016) and the proposed procedures. It is noted that while all three procedures provide adequate strength predictions for slender-web members in the plateau FLB region (Figure 20), the predictions start to become slightly un-conservative in the plateau FLB region of noncompact and compact web sections (see Figures 21 and 22). The prediction for a compact-web section with $b_f / 2t_f = 7$ is 5 % un-conservative compared to the FEA test result (Figure 22) while it is 3.6 % un-conservative for the same section with a noncompact web (Figure 21). The plateau region in Figures 20 and 21 is not perfectly horizontal because of the varying R_{pc} and R_{pg} factors for noncompact- and slender-web sections respectively.

5.2 Investigation of Local-Global Buckling Interaction

In this section the results for each test case presented in Table 2 (Chapter 3) are followed by detailed discussions. The results are evaluated as a ratio between the FEA simulation capacity and the capacity predicted by the strength equations. This is denoted

as M_{FEA}/M_n where M_n corresponds to strength prediction by any one of the three procedures being evaluated, i.e., FPB-NLG, FPB-LG and AISC (2016) Specification. The solid markers in the respective plots in Cases 1 through 5 represent an LTB mode of failure while the hollow markers represent an FLB failure.

Case 1: Slender-flange – slender-web sections under uniform moment loading having $F_y = 60$ ksi

It is evident from Figure 23 that the FPB-NLG procedure gives the closest approximation with test simulations. FPB-LG gives somewhat conservative predictions while the AISC (2016) Specification predictions are most conservative at shorter unbraced lengths.

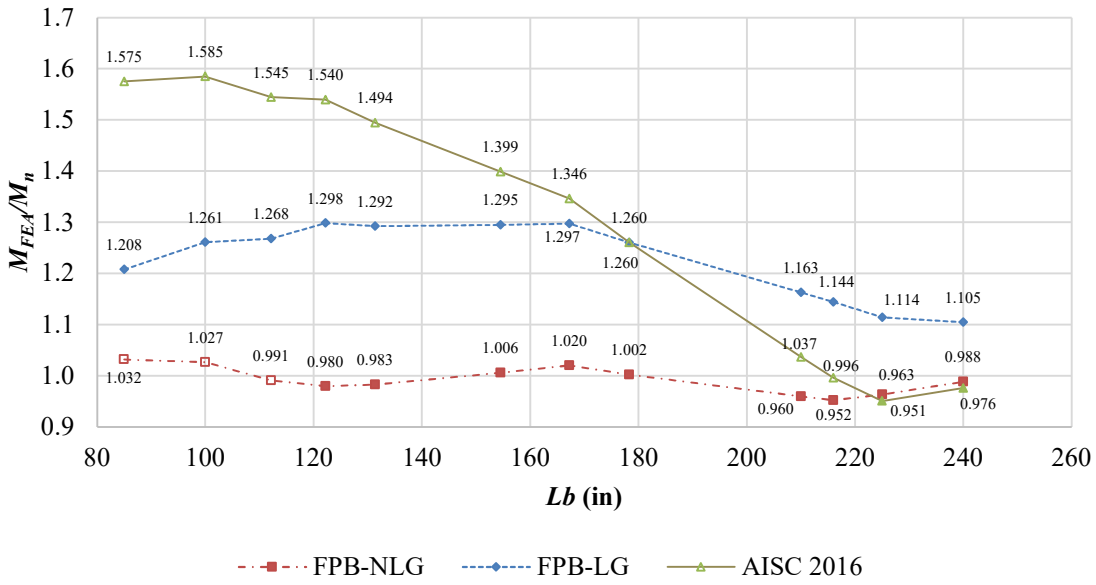

Figure 23: Comparison of M_{FEA}/M_n for the three procedures considered for Case 1 test members

The inelastic-elastic unbraced length limit (L_r) for this section is 216 in. It is observed that the FPB-NLG predictions become slightly unconservative near L_r, dropping down to the lowest strength ratio of 0.952 at L_r and then increasing to a ratio of 0.963 at (L_b = 225 in) > L_r. According to FPB-NLG, the first three data points represent an FLB limit state failure and the remaining are governed by LTB. For FPB-LG, however, all the data points correspond to an LTB failure. This is because FPB-LG uses an effective section in the LTB calculations. This lowers the LTB strength below the FLB limit state, resulting in an LTB failure mode. This is more conservative than the FPB-NLG calculation, which uses gross section properties throughout in the LTB strength calculation.

The AISC (2016) Specification predicts an FLB limit state for all the data points except for the last one which is governed by an LTB failure. This is because the AISC (2016) uses a theoretical elastic FLB resistance, which does not take into account the flange post-buckling reserve strength. This reduces the predicted FLB capacity significantly below the FLB capacity predicted by FPB-NLG and FPB-LG. For this reason, the FLB limit state governs in most cases for the AISC (2016) calculations. The last data point having a 0.952 strength ratio shows LTB failure. It is noted that while both the FPB-NLG and AISC (2016) Specifications use the same overarching concept in the LTB strength calculation, FPB-NLG recognizes an elastic-to-inelastic LTB transition at $0.5M_{yc}$ rather than $F_L S_{xc} = 0.7F_y S_{xc}$ in AISC (2016). This is the reason for different strength predictions between the two methodologies and it is evident that use of $0.5M_{yc}$ for the elastic-to-inelasitic transition gives a slightly better prediction. Figure 24 shows the deformed shape, scaled by a factor of 5.0, at failure plotted with the von Misses stress field at the top surface of shell elements

for a 210 inch long member. It can be seen that the flange shows significant distortion while the beam is also deforming in a global LTB shape.

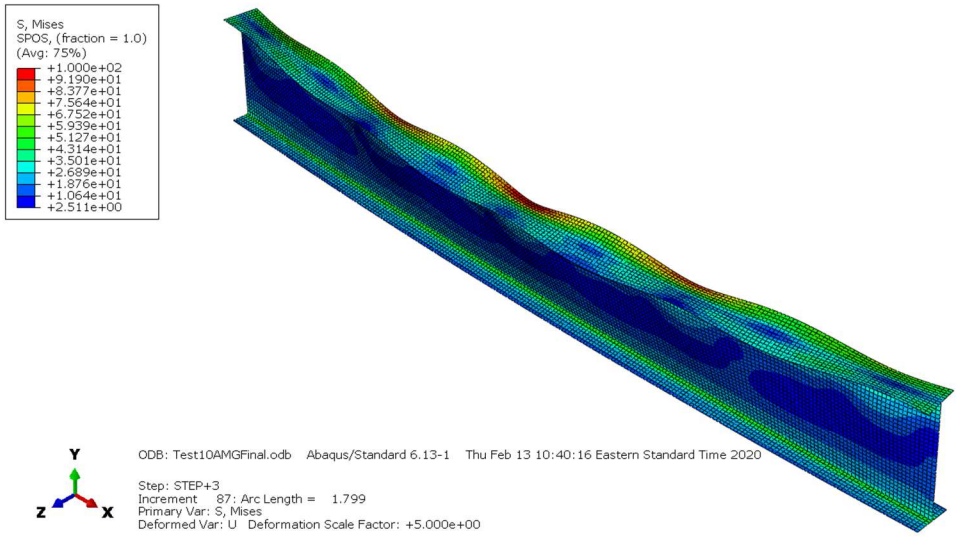

Figure 24: Deformed shape of UM-LB210-18-SW-60 at peak load plotted with von Mises stress contours (displacement scale factor = 5.0)

From these observations, it is apparent that these sections do not face any notable local-global buckling interaction since FPB-NLG, which uses a gross section in the LTB calculation, still gives good predictions compared to simulation results. This provides an indication that there is no or close to minimum reduction in the global LTB strength due to local buckling in these sections. It is worth noting that the slight dip in strength ratio of FPB-NLG in Figure 23 near L_r may be due to some local-global interaction. However, this does not seem to be significant and the strength predictions are still within an acceptable range. Therefore, it is recommended that the FPB-NLG procedure is suitable for 60 ksi members.

Case 2: Slender-flange – slender-web sections under uniform moment loading having $F_y = 100$ ksi

These sections are similar to the ones in Case 1, except that they are composed of 100 ksi steel. L_r for these members is 168 in. It can be observed from Figure 25 that their response is markedly different from the Case 1 sections.

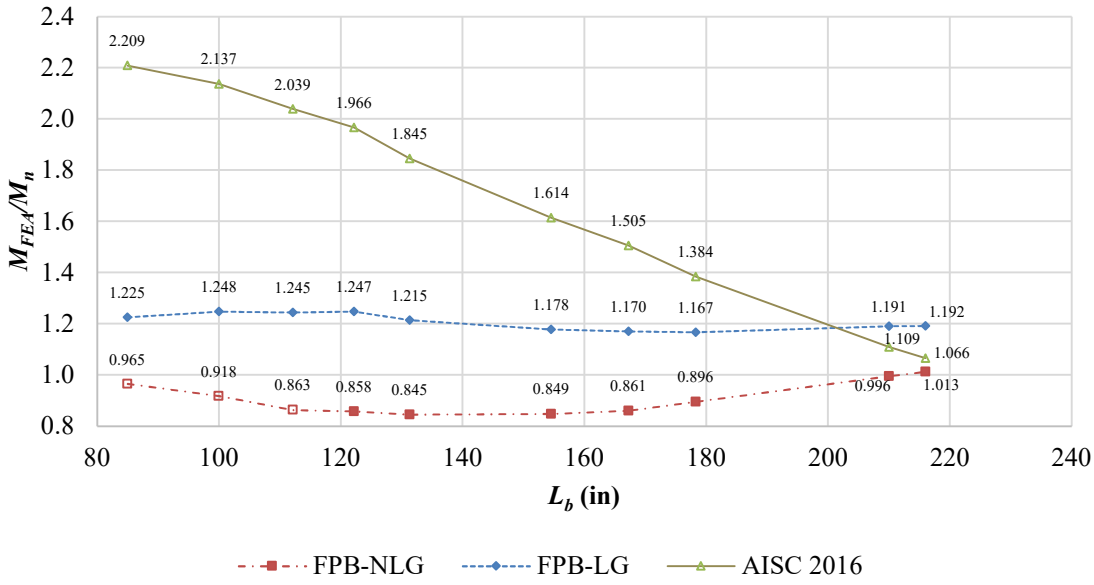

Figure 25: Comparison of M_{FEA}/M_n for the three methodologies considered for Case 2 test members

The FPB-NLG calculations, which gave very good predictions for 60 ksi members, are significantly unconservative for 100 ksi members. Meanwhile the FPB-LG calculations seem to give the best conservative approximation with FEA simulations. Comparison between FPB-NLG and FPB-LG predictions here shows that an effective LTB calculation employed in FPB-LG gives a much better representation of the actual behavior of the beams. The unconservative FPB-NLG predictions may be indicative of significant local-

global interaction over a large range of unbraced lengths. This behavior, however, is captured as intended using the effective LTB calculations in FPB-LG. The test section UM-LB154-18-SW-100 having an L_b of 154 inches seems to "feel" the largest impact from local-global interaction since it represents one of the lowest strength ratio of 0.849 for the FPB-NLG curve in Figure 25. The deformed shape, scaled by a factor of 5.0, at peak load of this member plotted with von Mises stress contours at the top surface of shell elements is shown in Figure 26.

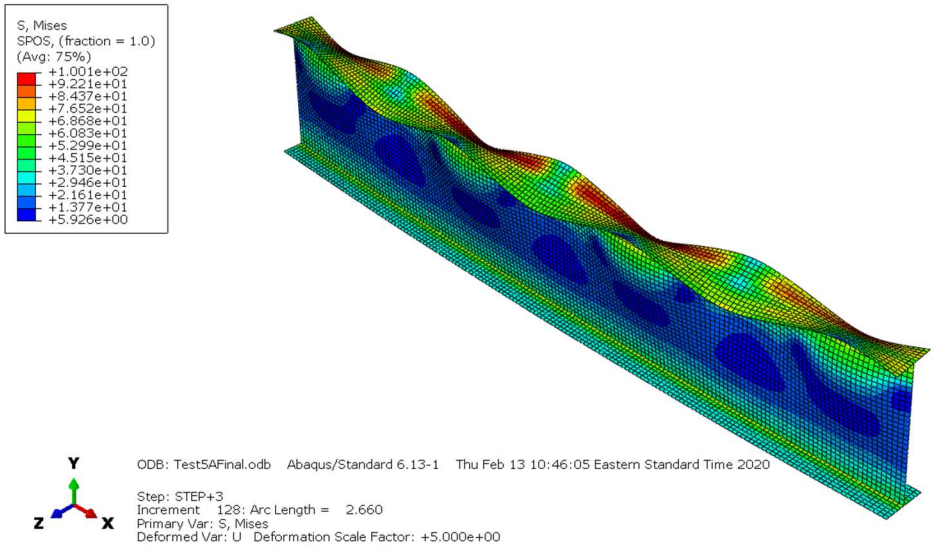

Figure 26: Deformed shape of UM-LB154-18-SW-100 test member at peak load plotted with von Mises stress contours (displacement scale factor = 5.0)

It is evident that the compression flange has undergone significant buckling deformations at the peak load. The FPB-NLG and FPB-LG procedures predict an LTB failure for this member. The reduced contribution of the compression flange to the global

strength of the member, due to extensive local buckling, is captured conservatively by the FBP-LG procedure in this case compared to the FPB-NLG procedure which assumes no local-global interaction.

The AISC (2016) Specification again gives highly conservative predictions especially for smaller unbraced lengths. This is again due to the conservative approximation of the FLB strength as the theoretical elastic strength, not considering the beneficial post-buckling strength. For 100 ksi sections, this conservatism may prove to be very costly.

Given these observations, the FPB-LG procedure is recommended for strength prediction of these 100 ksi steel members.

Case 3: Slender flange – compact web sections under uniform moment loading having F_y = 60 ksi

Similar to the Case 1 sections with 60 ksi steel, these compact-web sections give the best strength approximation using FPB-NLG as shown in Figure 27. The L_r for these members is 269 in. There is a slight dip in strength ratios for the FPB-NLG curve for the test member UM-LB260-18-CW-60 near L_r which may be indicative of some small local-global interaction, however, the predictions are still on the conservative side. FPB-LG, with its implementations of an effective LTB, under-predicts the LTB strength quite significantly especially at shorter unbraced lengths. This conservatism becomes progressively smaller as the effective width, b_e, approaches the full flange width at longer unbraced lengths.

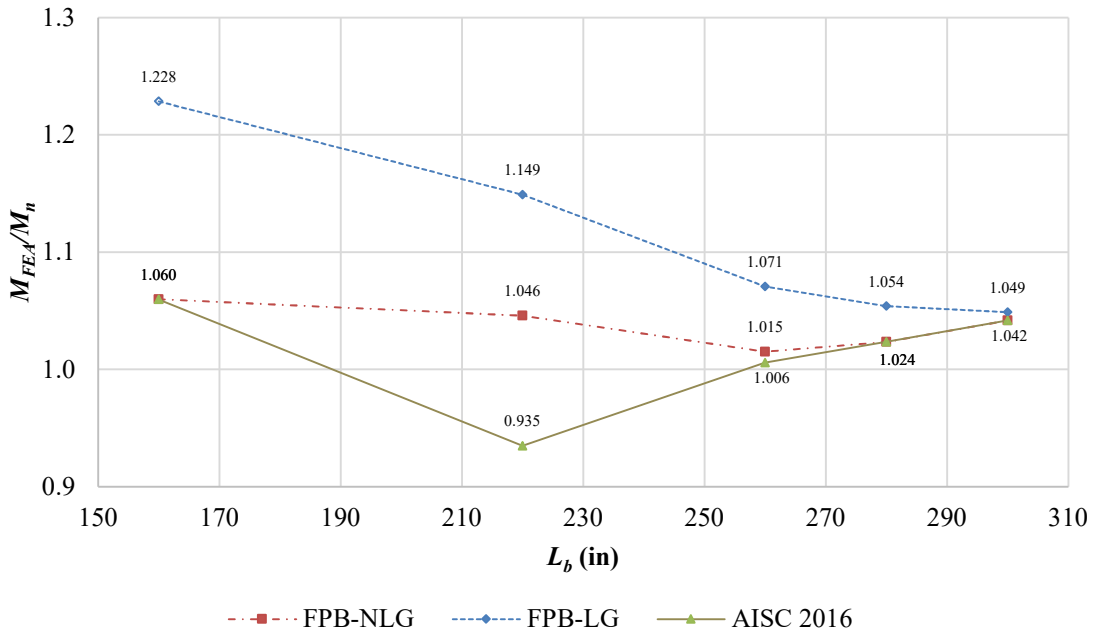

Figure 27: Comparison of M_{FEA}/M_n for the three methodologies considered for Case 3 test members

The AISC (2016) Specification gives the most erratic prediction in this case. Apart from the first data point which fails in FLB, the remaining points fail in LTB mode as per AISC (2016). The Specification over-predicts the inelastic LTB strength for L_b = 220 in. This same member (L_b = 220 in.) has a much better strength prediction using the FPB-NLG calculations, which use an elastic-to-inelastic LTB transition at $0.5M_{yc}$ instead of at $F_L S_{xc}$ = $0.7F_y S_{xc}$ used in AISC (2016). The last two data points represent elastic LTB failure. Therefore, the AISC (2016) and FPB-NLG predictions are the same for these points since they utilize the same strength equations.

The deformed shape, scaled by a factor of 5.0, at peak load plotted with a von Mises stress field is shown in Figure 28. It is evident that the beam is failing predominantly in

LTB and the compression flange is not undergoing significant local buckling deformations.

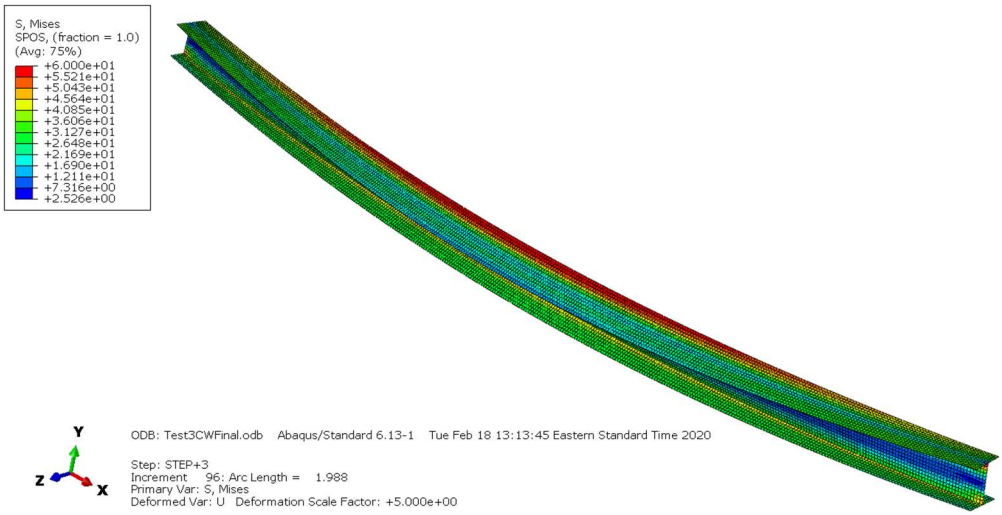

Figure 28: Deformed shape of UM-LB260-18-CW-60 test member at peak load plotted with von Mises stress contours (displacement scale factor = 5.0)

Given these observations, the FPB-NLG procedure is recommended for strength prediction of these 60 ksi steel members.

Case 4: Slender-flange – compact-web sections under uniform moment loading having F_y = 100 ksi

Similar to the 100 ksi sections in Case 2, these compact-web members have strength predictions closest to the FEA simulation results when using the FPB-LG procedure as evident from Figure 29. The L_r for these members is 199 in. FPB-NLG procedure gives unconservative estimates for this case while the FPB-LG procedure seems to capture the loss in global strength due to local-global interaction as intended.

The AISC (2016) Specification is again highly conservative at smaller unbraced lengths for this case due to the use of theoretical elastic buckling resistance for FLB strength prediction for slender flanges.

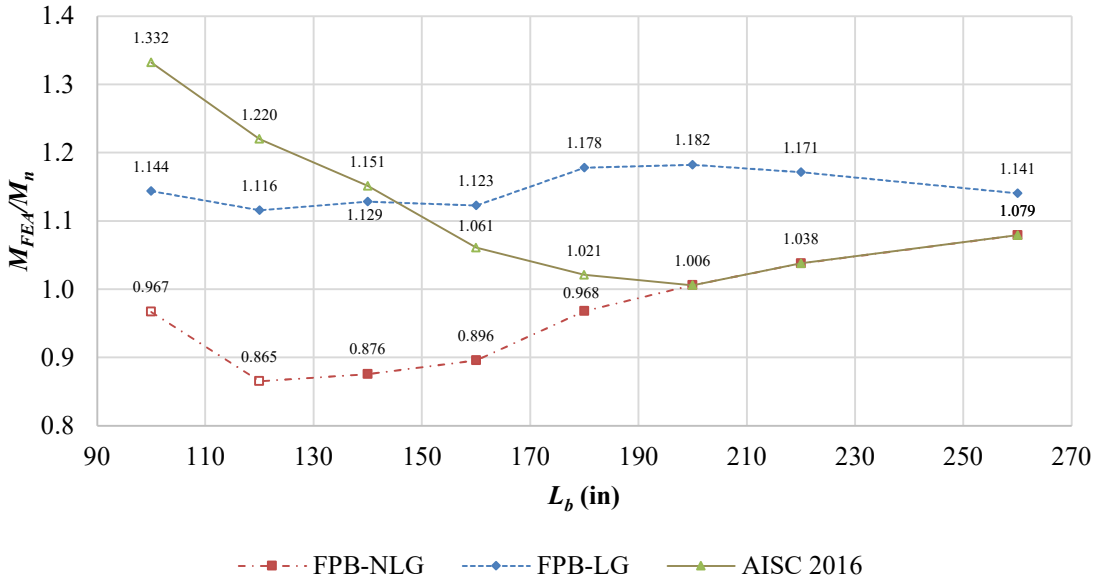

Figure 29: Comparison of M_{FEA}/M_n for the three methodologies considered for Case 4 test members

The extensive buckling of the compression flange at peak load for a representative UM-L140-18-CW-100 test member is illustrated in the scaled deformed shape plotted with von Mises stress field in Figure 30.

Both the FPB-NLG and FPB-LG procedures predict an LTB failure for the member in Figure 30. The strength prediction by FPB-LG is more accurate since it captures the loss of the strength contribution from the compression flange to the global LTB resistance due to extensive local buckling of the flange.

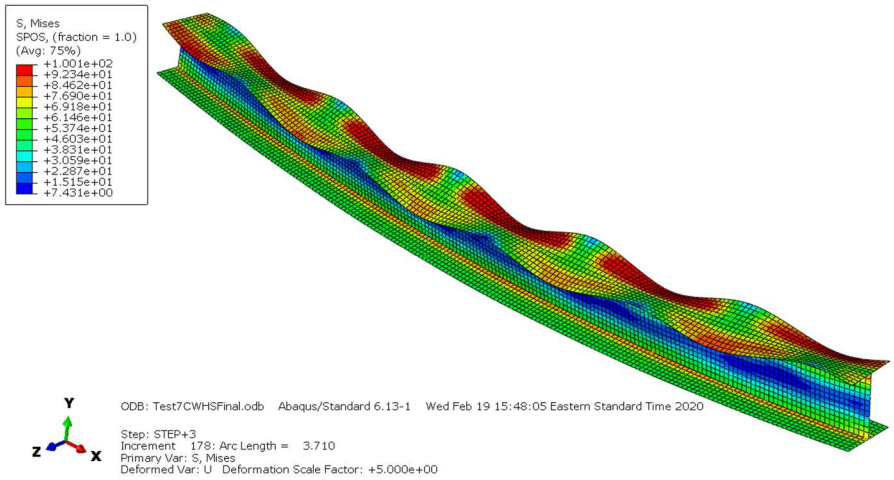

Figure 30: Deformed shape of UM-LB140-18-CW-100 test member at peak load plotted with von Mises stress contours (displacement scale factor = 5.0)

Given these observations, the FPB-NLG procedure is recommended for strength prediction of these 100 ksi steel members.

Case 5: Slender-flange – slender-web sections under a linear moment gradient having $F_y = 60$ ksi

These 60 ksi test members are subjected to a linear moment gradient effect, with the moment diagram equal to zero at one member end and maximum at the other. This effect increases the calculated LTB strength by a factor of $C_b = 1.75$; therefore, the FLB limit governs for all these sections except for the predictions for the last three data points by FPB-LG where LTB failure governs (see Figure 31).

Expectedly, the strength predictions by FPB-NLG and FPB-LG. which utilize the post-buckling FLB strength, overlap for all member unbraced lengths where FLB limit governs. The AISC (2016) predictions are once again highly conservative, by 31.3% in this case

compared to FLB predictions by FPB-LG and FPB-NLG, due to the idealization of slender FLB strength as theoretical elastic resistance.

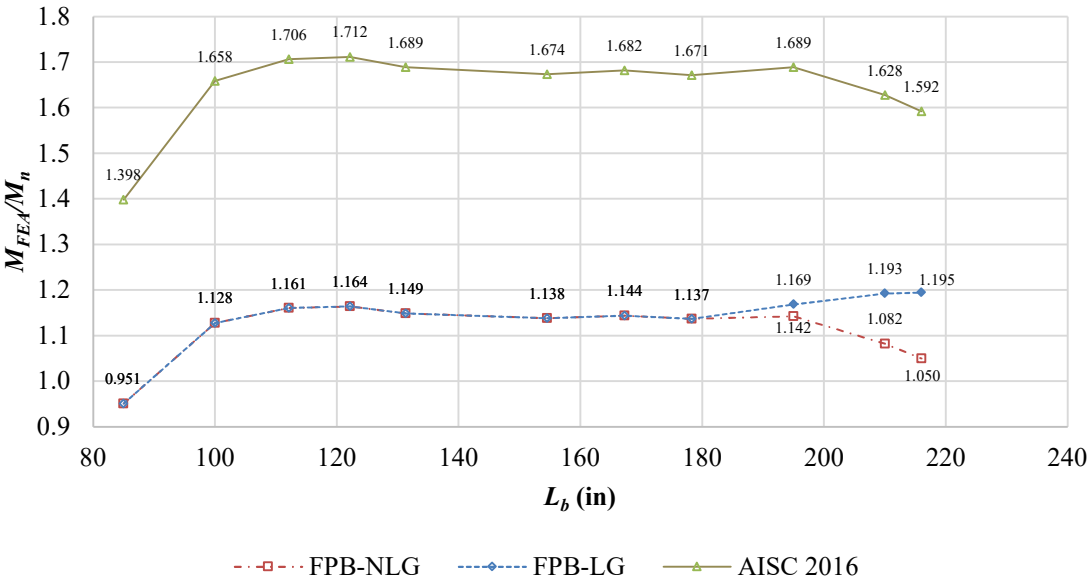

Figure 31: Comparison of M_{FEA}/M_n for the three methodologies considered for Case 5 test members

A scaled deformed shape of a representative MG-LB178-18-SW-60 test member plotted with von Mises stress contours is shown in Figure 32.

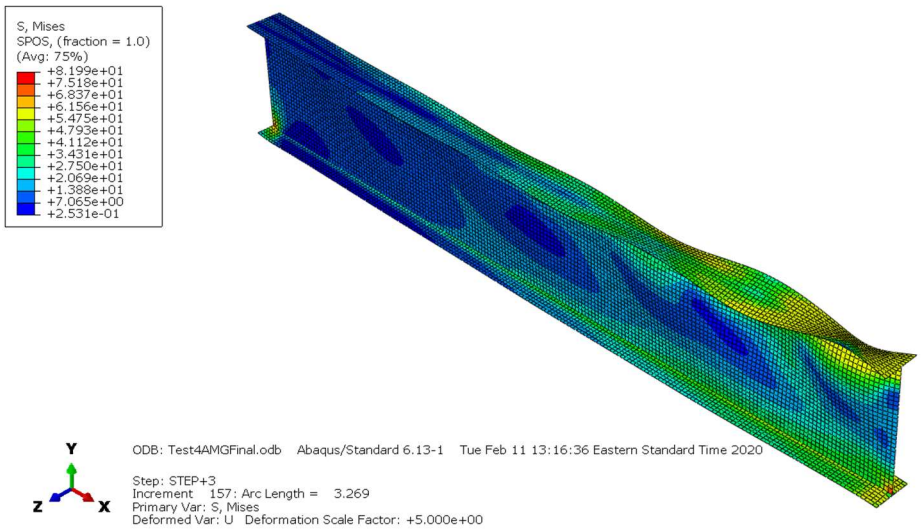

Figure 32: Deformed shape of MG-LB178-18-SW-60 test member at peak load plotted with von Mises stress contours (displacement scale factor = 5.0)

CHAPTER 6. CONCLUSIONS

This research contributes to an improved characterization of the flexural response of I-section beams with slender flange members. In light of the discussions in Chapter 5, the conclusions can be summarized in the following key points:

1. The proposed FPB-LG and FPB-NLG procedures account for the slender flange post-buckling strength of members. This gives substantial additional capacity compared to AISC (2016) Specification handling of FLB limit state for slender flanges, due to the recognition of significant post-buckling strength in the proposed procedures.
2. The FPB-LG and FPB-NLG procedures are somewhat conservative for compact- and noncompact-web sections with flanges having intermediate slenderness values. These predictions can be improved, potentially, by using a larger plate local plate buckling coefficient, k_c, than expressed in the AISC (2016) equations.
3. The FPB-NLG procedure accounts for the post-buckling strength of slender flanges but does not characterize the presence of any local-global buckling interaction (in terms of impact of the flange local buckling on the global lateral-torsional buckling strength). From the parametric FEA study on slender-flange sections ($b_f/2t_f = 18$), it is observed that this procedure gives the closest strength predictions for 60 ksi steel sections. However, for 100 ksi sections, this approach gives unconservative predictions. This is believed to be an indication of significant local-global buckling

interaction in 100 ksi steels. Therefore, the proposed FPB-NLG procedure is recommended for sections with 60 ksi yield stress or less.

4. The FPB-LG procedure accounts for the post-buckling strength of slender flanges as well as the presence of local-global buckling interaction. This interaction is handled through a reduction in the global LTB capacity of the member. This procedure seems to give the closest conservative approximation for slender-flange ($b_f/2t_f = 18$) members with a yield stress of 100 ksi while predictions for 60 ksi steel are somewhat conservative. Therefore, the proposed FPB-LG procedure is recommended for sections with 100 ksi yield stress.

For future studies, it is recommended that steels with yield stresses in the range between 60 ksi and 100 ksi be studied to investigate the maximum yield stress where strength predictions by the FPB-NLG procedure remain adequate. Higher strength steels beyond 100 ksi may also be studied to evaluate the suitability of the FPB-LG procedure for these steels.

Also, this study focuses only on doubly symmetric sections. It is recommended to evaluate these proposed procedures for singly symmetric I-section beams as well. Moreover, experimental testing should be performed to validate the findings in this study before consideration in future AISC Specification revision cycles.

APPENDIX A. FLOWCHARTS FOR METHODOLOGIES STUDIED FOR FLEXURAL STRENGTH CALCULATIONS

A.1 FPB-NLG Procedure: Flexural Strength Calculations

The following flowcharts (Figures 33 through 36) summarize the proposed FPB-NLG procedure.

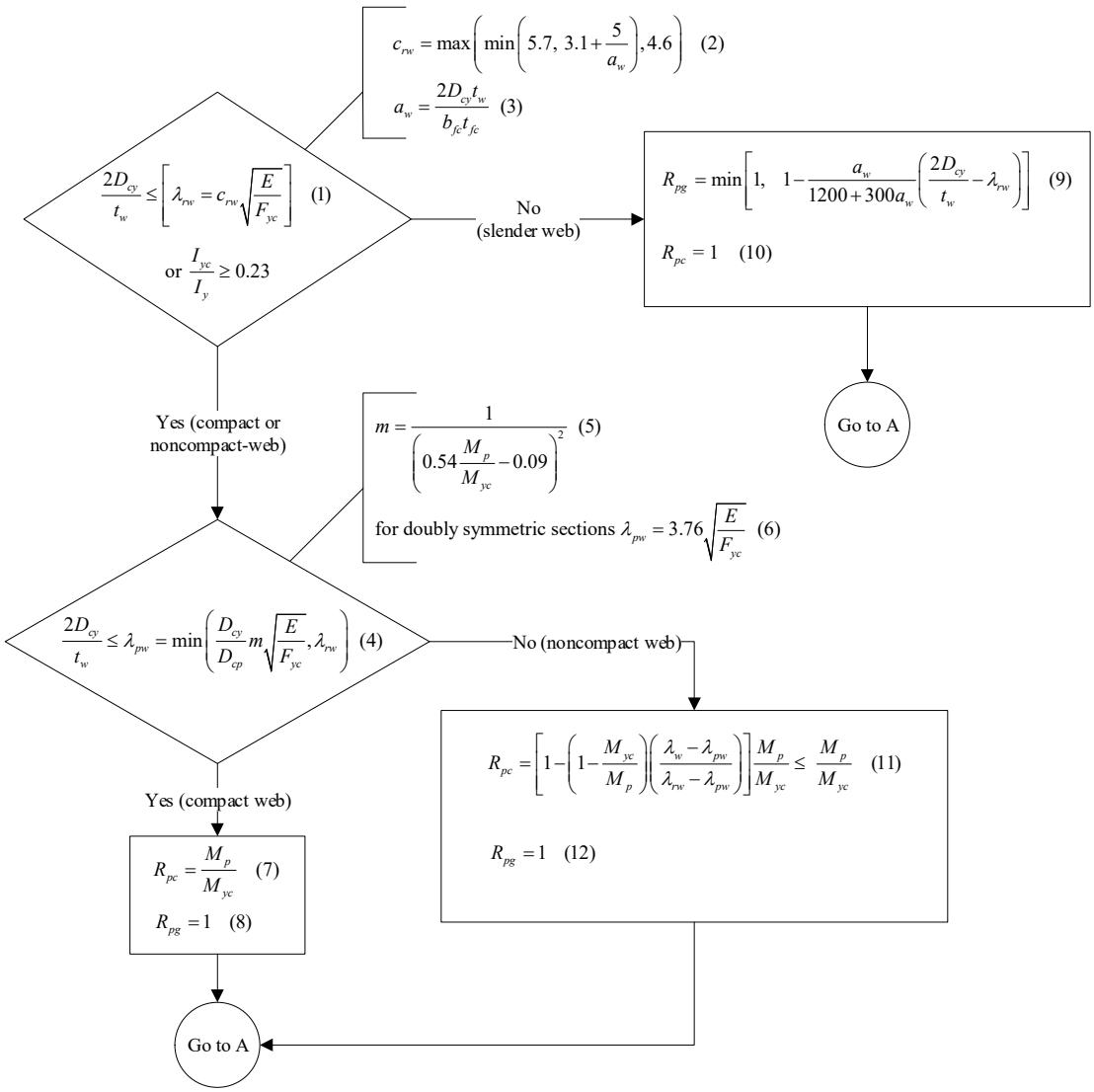

Figure 33: Calculation of web slenderness parameters R_{pc} and R_{pg}

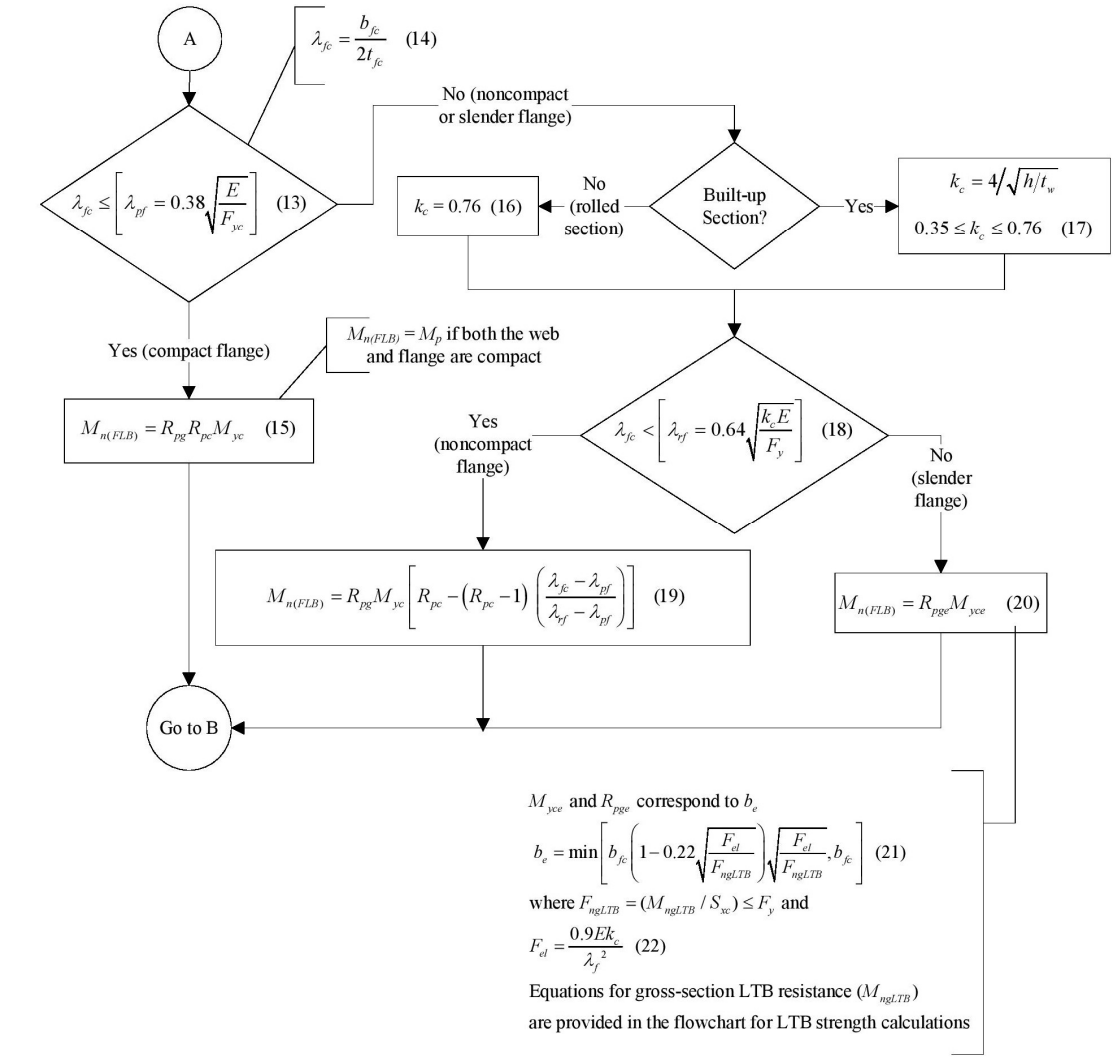

Figure 34: Flange local buckling strength calculations

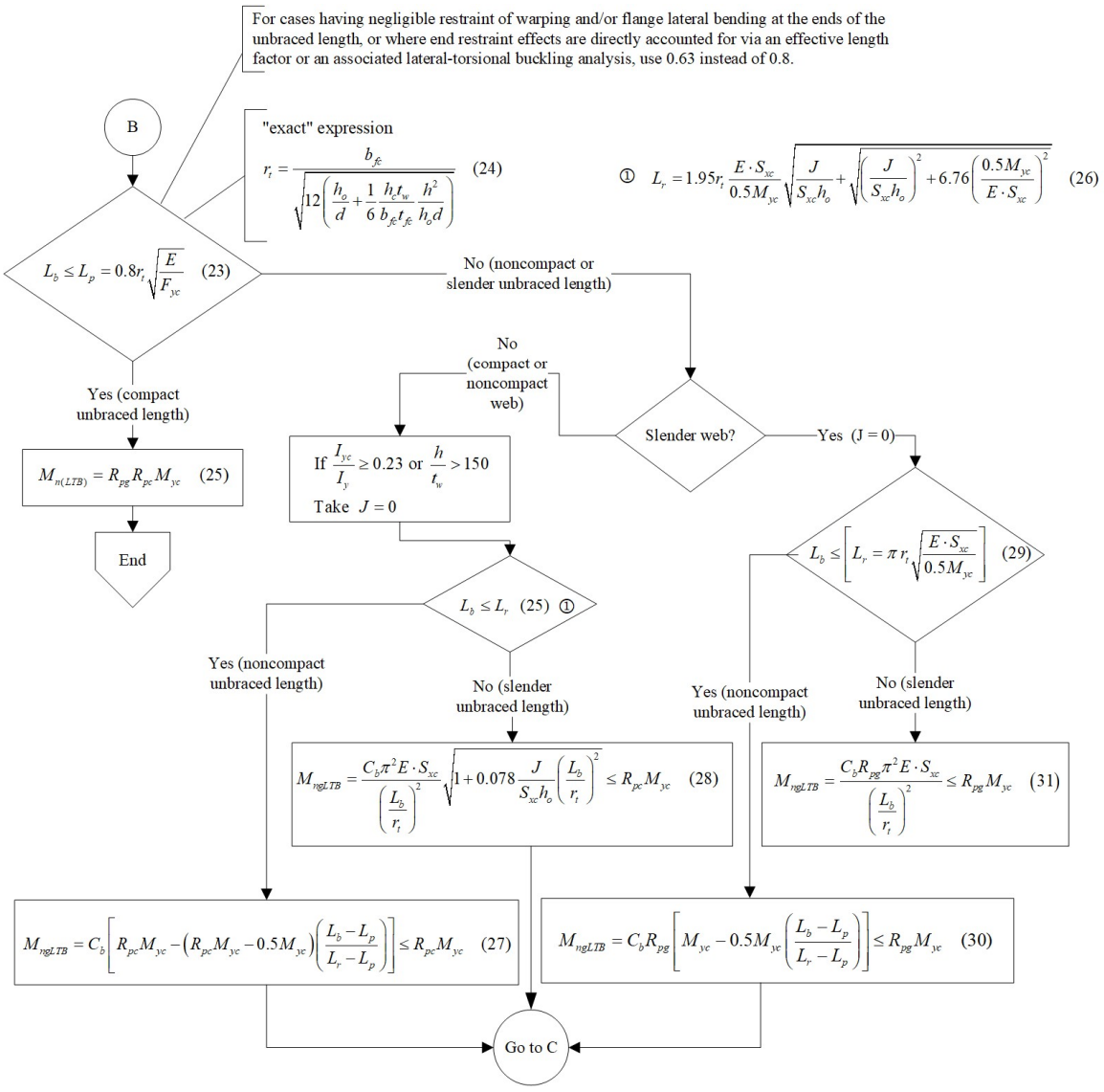

Figure 35: Lateral-torsional buckling strength calculations, FPB-NLG procedure

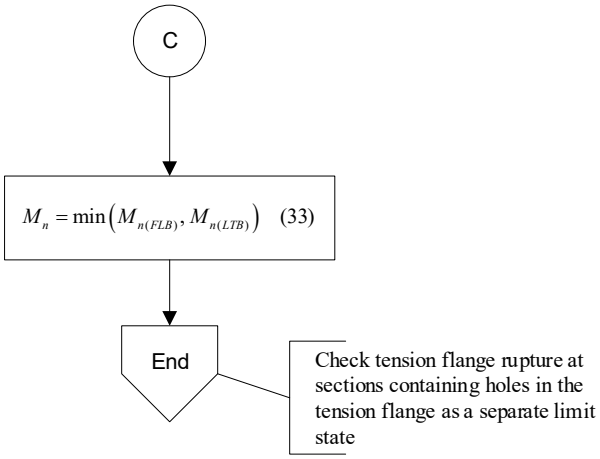

Figure 36: Completion of flexural resistance calculations

A.2 FPB-LG Procedure: Flexural Strength Calculations

The FPB-LG and FPB-NLG procedures differ only in the calculation of LTB strengths. Figure 37 outlines the LTB calculations for the FPB-LG procedure while Figures 33, 34 and 36 in Section A.1 provide the remaining flexural strength calculations.

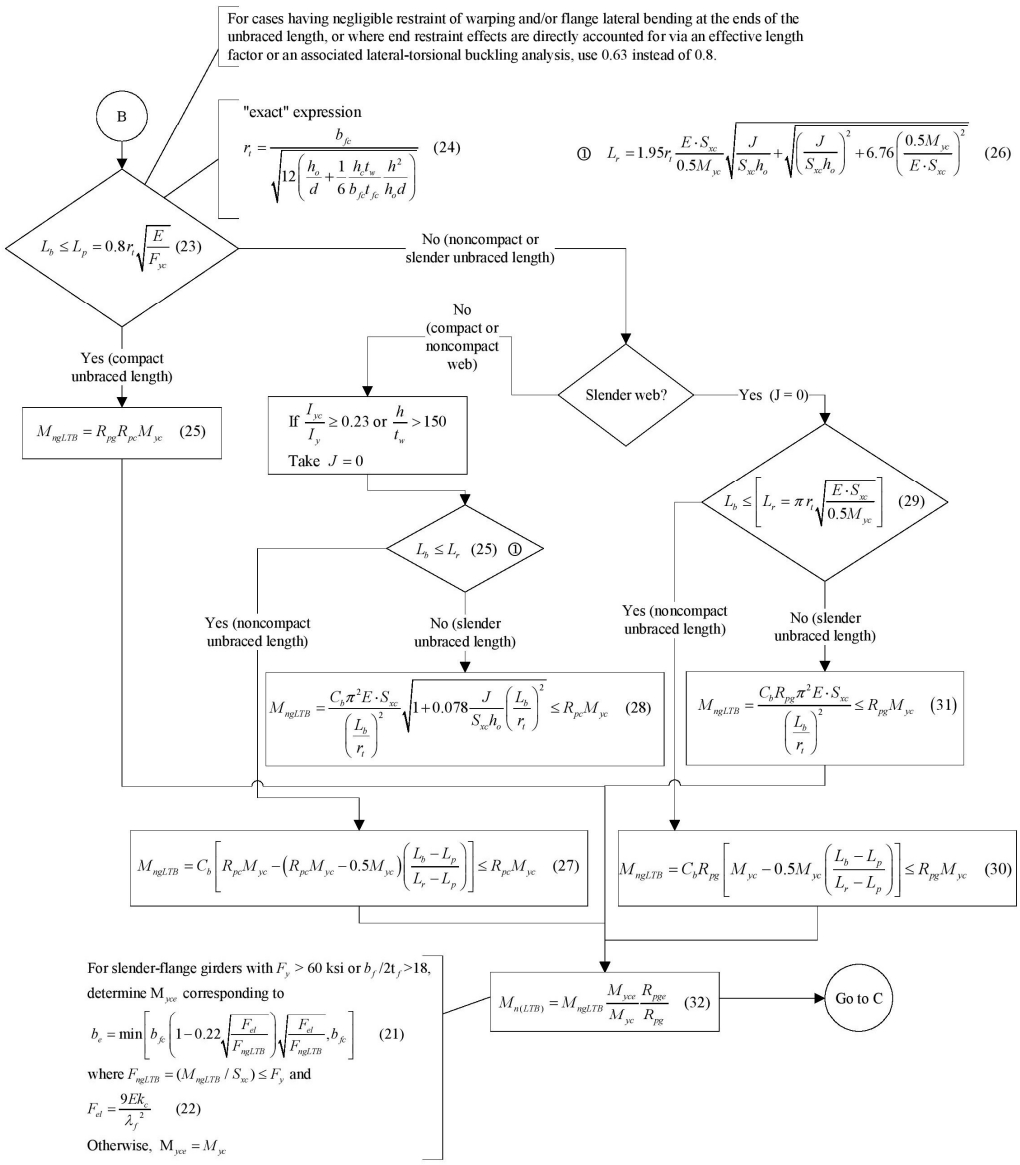

Figure 37: Lateral-torsional buckling strength calculations for FPB-LG procedure

A.3 AISC (2016) Specification: Flexural Strength Calculations

The following flowcharts (Figures 38 through 41) summarize the flexural design of welded I-section beams considered in this study in accordance with the AISC (2016) Specification. The calculations are shown in an overall "unified" format, similar to the synthesis of the AISC (2016) Section F4 and F5 provisions by White (2008) and to the application of the AISC (2016) equations in AISC/MBMA Design Guide 25 (White and Jeong, 2020). That is, the flowcharts do not give separate calculations for the different classifications in Sections F2 through F5, but rather give an equivalent single set of calculations that apply to all these sections.

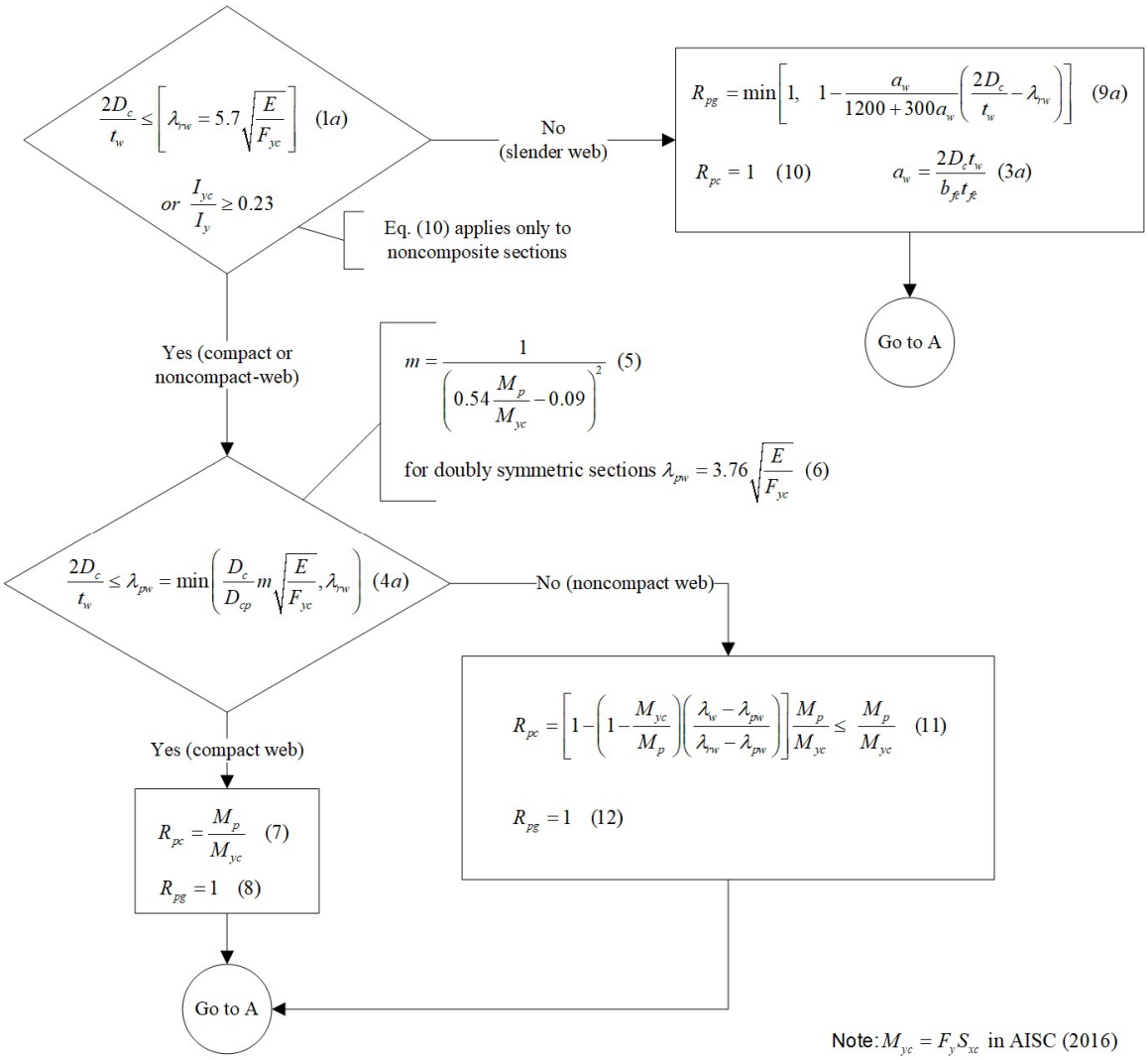

Figure 38: Calculation of web slenderness parameters R_{pc} and R_{pg} as per AISC (2016)

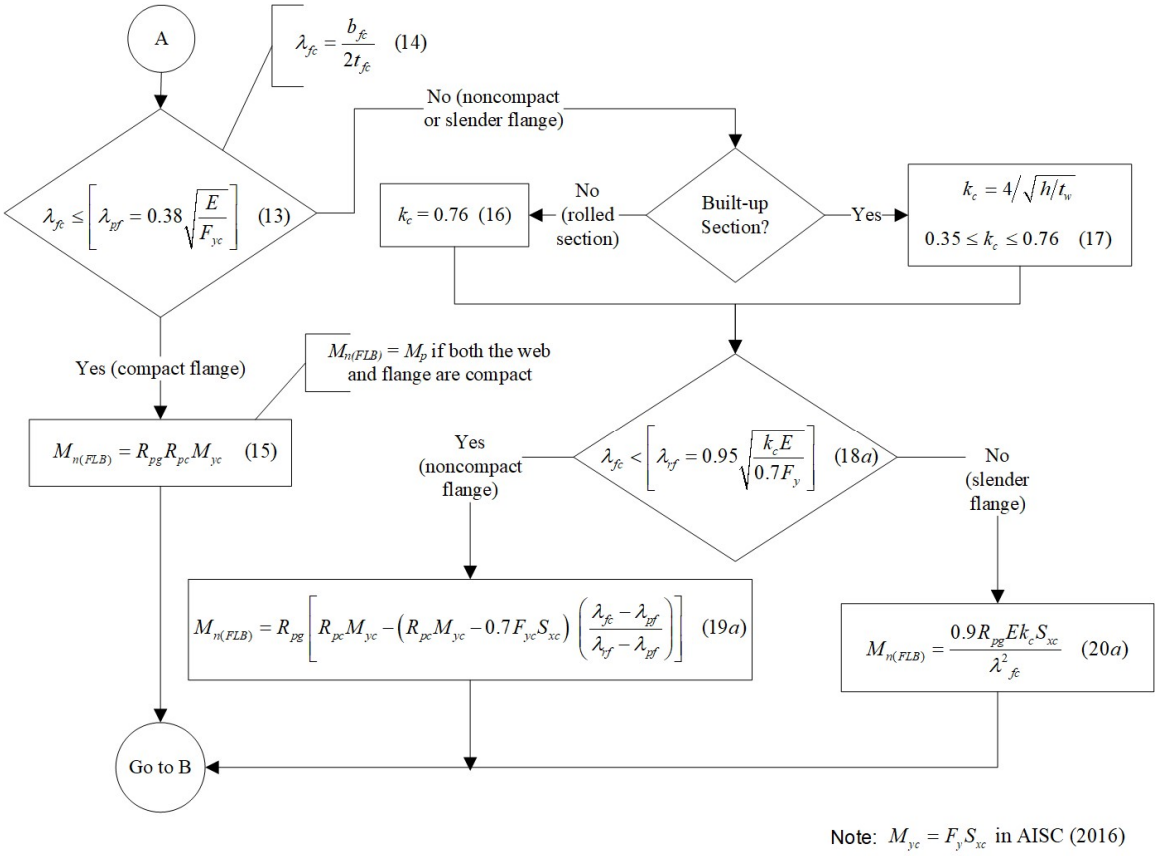

Figure 39: Flange local buckling strength calculations as per AISC (2016)

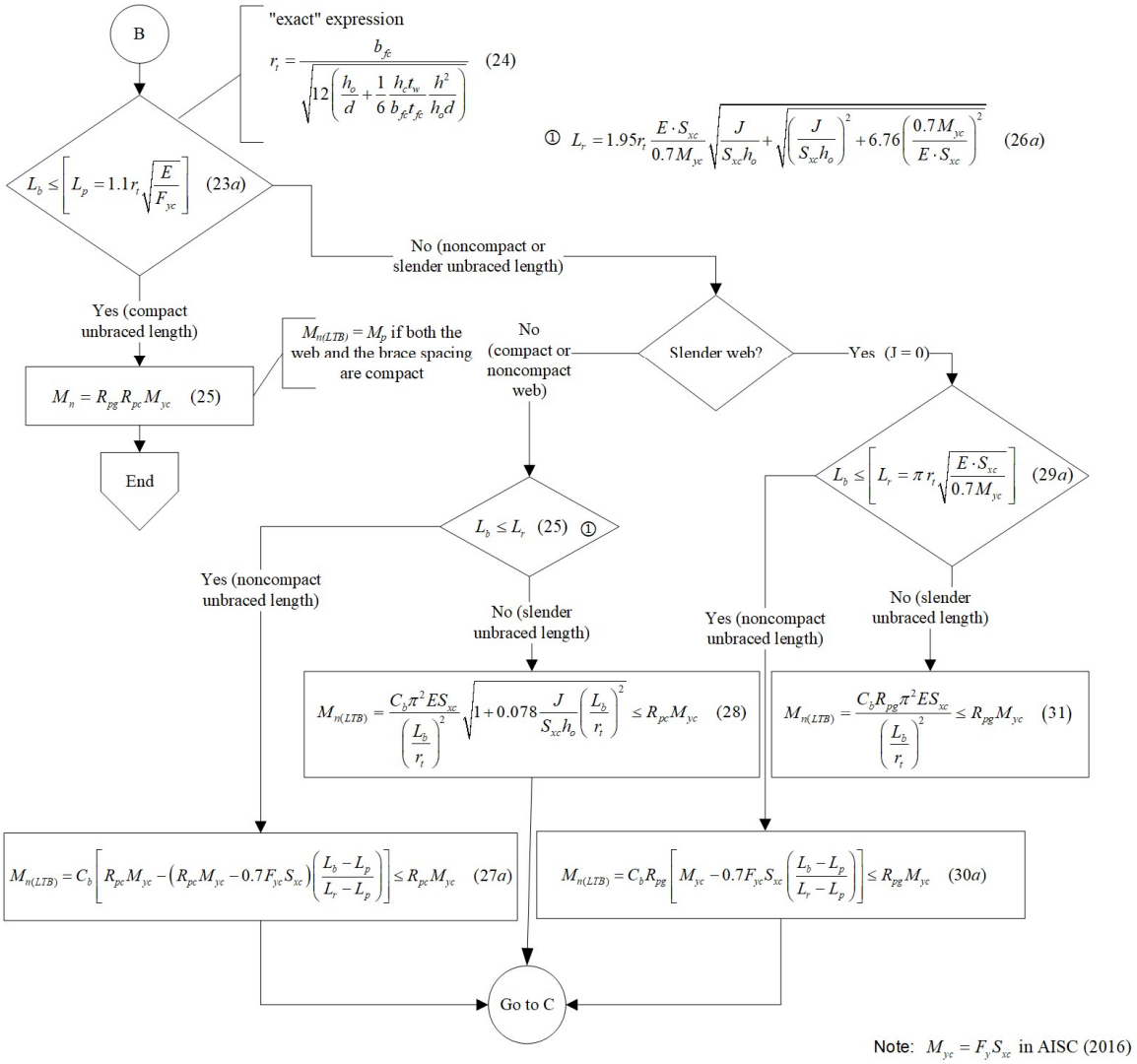

Figure 40: Lateral-torsional buckling strength calculations as per AISC (2016)

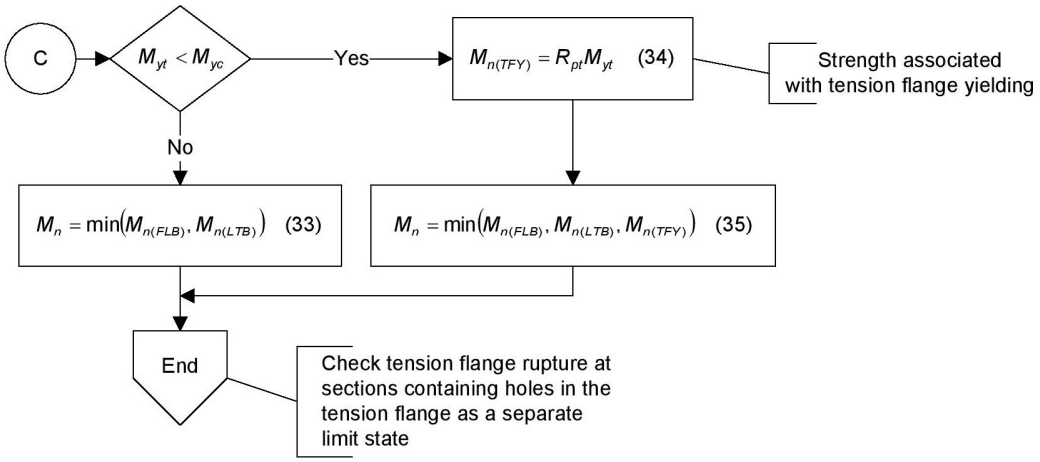

Figure 41: TFY limit state check and end of flexural strength calculations

APPENDIX B. FLEXURAL STRENGTH CALCULATIONS FOR A REPRESENTATIVE I-SECTION PER FPB-NLG, FPB-LG AND AISC (2016) SPECIFICATION PROCEDURES

This section outlines the flexural strength calculations for a representative test section in accordance with the FPB-NLG, the FPB-LG and AISC (2016) Specification procedures in Sections B.1, B.2 and B.3 respectively. The flowcharts in Appendix A guide these calculations.

Section Name: UM-LB210-18-SW-60 (Doubly Symmetric Section)

Section Properties

$b_f := 9in$ $t_f := 0.25in$ $h := 28in$ $t_w := 0.1875in$

$L_b := 210in$ $C_b := 1$ $F_y := 60\frac{kip}{in^2}$ $E := 29000\frac{kip}{in^2}$

$d := h + 2\cdot t_f = 28.5\cdot in$ $h_o := h + t_f = 28.25\,in$

Elastic Cross-section Properties

$A := h\cdot t_w + 2\cdot b_f\cdot t_f = 9.75\cdot in^2$ $A_f := b_f\cdot t_f = 2.25\cdot in^2$ $A_w := h\cdot t_w = 5.25\cdot in^2$

$$D_{cy} := \frac{A_f\cdot\left(\frac{-t_f}{2}\right) + A_f\cdot\left(h + \frac{t_f}{2}\right) + A_w\cdot\frac{h}{2}}{A} = 14\cdot in$$

$h_{cy} := 2\cdot D_{cy} = 28\cdot in$

$$I_x := \frac{b_f\cdot t_f^{\,3}}{12} + A_f\cdot\left(D_{cy} + \frac{t_f}{2}\right)^2 + \frac{b_f\cdot t_f^{\,3}}{12} \ldots + A_f\cdot\left(h - D_{cy} + \frac{t_f}{2}\right)^2 + \frac{t_w\cdot h^3}{12} + A_w\cdot\left(D_{cy} - \frac{h}{2}\right)^2 = 1.241\times 10^3\cdot in^4$$

$S_x := \frac{I_x}{D_{cy} + t_f} = 87.077\,in^3$ $I_{yc} := \frac{t_f\cdot b_f^{\,3}}{12} = 15.188\,in^4$

$$I_y := I_{yc} + \frac{h \cdot t_w^{\,3}}{12} + \frac{t_f \cdot b_f^{\,3}}{12} = 30.39\,in^4 \qquad \frac{I_{yc}}{I_y} = 0.5$$

$$r_{te} := \frac{b_f}{\sqrt{12\left(\frac{h_o}{d} + \frac{D_{cy} \cdot t_w \cdot h^2}{3 \cdot b_f \cdot t_f \cdot h_o \cdot d}\right)}} = 2.22\,in \qquad J := \frac{h \cdot t_w^{\,3}}{3} + \frac{2b_f \cdot t_f^{\,3}}{3} \cdot \left(1 - 0.63 \cdot \frac{t_f}{b_f}\right) = 0.154\,in^4$$

$$M_{yc} := F_y \cdot S_x = 5.225 \times 10^3 \cdot kip \cdot in$$

For doubly symmetric sections

Plastic Cross-section Properties

Since this is a doubly symmetric section, the location of Plastic Neutral Axis (PNA) is at the center of the section, i.e., in the web.

$$D_{cp} := \frac{t_f \cdot b_f - t_f \cdot b_f + t_w \cdot h}{2 \cdot t_w} = 14\,in$$

$$M_p := 2 \cdot A_f \cdot F_y \cdot \left(D_{cp} + \frac{t_f}{2}\right) + 2D_{cp} \cdot t_w \cdot F_y \cdot \left(\frac{D_{cp}}{2}\right) = 6.019 \times 10^3 \cdot kip \cdot in$$

Flexural strength calculations in accordance with FPB-NLG, FPB-LG and AISC (2016) Specification procedures are presented in the following Sections B.1, B.2 and B.3 respectively.

B.1 Procedure I: FPB-NLG Approach accounting for Slender Flange Post-Buckling Strength with no Local-Global Buckling Interaction

Web Local Buckling Parameters

$$\lambda_w := \frac{h}{t_w} = 149.333$$

$$\lambda_{pw} := 3.76\sqrt{\frac{E}{F_y}} = 82.663$$ For doubly symmetric sections

$$a_w := \frac{h_{cy} \cdot t_w}{b_f \cdot t_f} = 2.333$$

$$c_{rw} := \max\left(\min\left(3.1 + \frac{5}{a_w}, 5.7\right), 4.6\right) = 5.243$$

$$\lambda_{rw.new} := c_{rw} \cdot \sqrt{\frac{E}{F_y}} = 115.263$$

$\lambda_w > \lambda_{rw.new} = 1$ Therefore, the web is slender

$R_{pc} := 1$ For slender webs

$$R_{pg} := \min\left[1, 1 - \frac{a_w}{1200 + 300 \cdot a_w} \cdot \left(2 \cdot \frac{D_{cy}}{t_w} - \lambda_{rw.new}\right)\right] = 0.958$$

Flange Local Buckling Parameters

$$\lambda_f := \frac{b_f}{2 \cdot t_f} = 18$$

$$\lambda_{pf} := 0.38\cdot\sqrt{\frac{E}{F_y}} = 8.354$$

$$k_c := \max\left(\min\left(\frac{4}{\sqrt{\frac{h}{t_w}}}, 0.76\right), 0.353\right) = 0.353$$

$$\lambda_{rf.new} := 0.64\cdot\sqrt{\frac{k_c\cdot E}{F_y}} = 8.36$$

$\lambda_f > \lambda_{rf.new} = 1$ Therefore, flange is slender

LTB Calculation not accounting for local-global buckling interaction

$L_b = 210\cdot in$ Given unbraced length

$L_p := 0.63\cdot r_{te}\cdot\sqrt{\frac{E}{F_y}} = 30.745 in$ This recommended equation for L_p is used since the member ends have negligible warping restraint in the FEA model

$L_r := \pi\cdot r_{te}\cdot\sqrt{\frac{E\cdot S_x}{0.5\cdot M_{yc}}} = 216.817 in$ J=0 since the web is slender

$L_p < L_b < L_r = 1$ Section has a non-compact unbraced length

Calculating LTB strength for gross area:

$$M_{ngLTB} := \min\left[C_b\cdot R_{pg}\cdot\left[M_{yc} - 0.5\cdot M_{yc}\cdot\left(\frac{L_b - L_p}{L_r - L_p}\right)\right], R_{pg}\cdot M_{yc}\right] = 2.595\times 10^3\cdot kip\cdot in$$

$$M_{nLTB} := M_{ngLTB} = 2.595\times 10^3\cdot kip\cdot in$$

FLB Calculation with Effective Width Approach For Slender Flanges (Not Applicable for Compact and Non-Compact Flanges)

$$F_{el} := \frac{0.9 \cdot E \cdot k_c}{\lambda_f^{\,2}} = 28.436 \frac{kip}{in^2}$$

$$b_e := \min\left[b_f , b_f \cdot \left(1 - 0.22 \cdot \sqrt{\frac{F_{el} \cdot S_x}{M_{ngLTB}}} \right) \cdot \sqrt{\frac{F_{el} \cdot S_x}{M_{ngLTB}}} \right] = 6.902 \cdot in$$ Effective width of compression flange

$$\frac{b_e}{b_f} = 0.767 \qquad A_{fe} := b_e \cdot t_f = 1.726 in^2 \qquad A_e := b_e \cdot t_f + h \cdot t_w + b_f \cdot t_f = 9.226 in^2$$

Effective Elastic Section Properties

$$D_{cye} := \frac{A_{fe} \cdot \left(\frac{-t_f}{2} \right) + A_f \cdot \left(h + \frac{t_f}{2} \right) + A_w \cdot \frac{h}{2}}{A_e} = 14.803 in$$

$$I_{xe} := \frac{b_e \cdot t_f^{\,3}}{12} + A_{fe} \cdot \left(D_{cye} + \frac{t_f}{2} \right)^2 + \frac{b_f \cdot t_f^{\,3}}{12} + A_f \cdot \left(h - D_{cye} + \frac{t_f}{2} \right)^2 + \frac{t_w \cdot h^3}{12} \ldots + A_w \cdot \left(D_{cye} - \frac{h}{2} \right)^2 = 1130.269 in^4$$

$$S_{xe} := \frac{I_{xe}}{D_{cye} + t_f} = 75.087 in^3$$

$$M_{yce} := F_y \cdot S_{xe} = 4.505 \times 10^3 \cdot kip \cdot in \qquad h_{cye} := 2 \cdot D_{cye} = 29.606 in$$

Web Local Buckling Parameters for Effective Section

$$\lambda_{we} := \frac{h_{cye}}{t_w} = 157.897$$

$$\lambda_{pw} := 3.76\sqrt{\frac{E}{F_y}} = 82.663$$ For doubly symmetric sections

$$a_{we} := \frac{h_{cye} \cdot t_w}{b_e \cdot t_f} = 3.217$$

$$c_{rwe} := \max\left(\min\left(3.1 + \frac{5}{a_{we}}, 5.7\right), 4.6\right) = 4.654$$

$$\lambda_{rwe} := c_{rwe} \cdot \sqrt{\frac{E}{F_y}} = 102.324$$

$$\lambda_{we} > \lambda_{rwe} = 1$$ Therefore, the web is slender

$$R_{pge} := \min\left[1, 1 - \frac{a_{we}}{1200 + 300 \cdot a_{we}} \cdot \left(2 \cdot \frac{D_{cye}}{t_w} - \lambda_{rwe}\right)\right] = 0.917$$

Post-buckled FLB Strength

$$M_{nFLB} := R_{pge} \cdot M_{yce} = 4.133 \times 10^3 \cdot kip \cdot in$$

This is the FLB strength for slender flanges accounting for flange post-buckling strength

Strength of Section

$$M_n := \min\left(M_{nFLB}, M_{nLTB}\right) = 2.595 \times 10^3 \cdot kip \cdot in$$

B.2 Procedure II: FPB-LG Approach accounting for Slender Flange Post-Buckling Strength with Local-Global Buckling Interaction

The FPB-LG procedure characterizes the local-global buckling interaction through an effective width procedure in LTB calculations for slender flanges. The section properties and FLB calculations are handled in the same way as in the FPB-NLG procedure (accounting for slender flange post-buckling strength). For this reason, the FLB calculations are not repeated in this section. The FLB strength for the given section is taken from the FLB calculations in the FPB-NLG procedure (Appendix B.1), i.e., $M_{nFLB} = 4.133 \times 10^{3} \cdot kip \cdot in.$

The LTB calculation using effective width approach for slender flanges is given below.

Note: The flowchart for FPB-LG procedure in Appendix A.2 recommends using this procedure for sections with $F_y \geq 60$ ksi and $b_f/2t_f \geq 18$. However, for illustration purposes, the FPB-LG procedure calculations are provided below for the test section considered in this Appendix.

LTB Calculation with Effective Width Approach for Slender Flanges accounting for local-global buckling interaction (Not Applicable for Compact and Non-Compact Flanges)

The effective section properties based on an effective width $b_e = 6.902 \cdot in$ calculated in Appendix B.1 for FLB post-buckling strength calculations are used for calculating the LTB strength based in this section.

$M_{ngLTB} = 2.595\times 10^{3}\cdot kip\cdot in$ Gross section LTB strength calculated in Appendix B.1

$R_{pg} = 0.958$ $R_{pge} = 0.917$ $M_{yc} = 5.225\times 10^{3}\ kip\cdot in$ $M_{yce} = 4.505\times 10^{3}\ kip\cdot in$

LTB strength of effective section for slender flanges

$$M_{nLTB} := M_{ngLTB}\cdot\frac{M_{yce}}{M_{yc}}\cdot\frac{R_{pge}}{R_{pg}} = 2.142\times 10^{3}\cdot kip\cdot in$$

This is the effective LTB strength of slender flange section accounting for local-global buckling interaction

Strength of Section

$$M_n := \min\left(M_{nFLB}, M_{nLTB}\right) = 2.142\times 10^{3}\cdot kip\cdot in$$

B3. AISC (2016) Specification Procedure

Web Local Buckling Parameters

$\lambda_w = 149.333$ $\lambda_{pw} = 82.663$ $a_w = 2.333$ Calculated previously

$$\lambda_{rw.AISC2016} := 5.7 \cdot \sqrt{\frac{E}{F_y}} = 125.314$$

$\lambda_w > \lambda_{rw.AISC2016} = 1$ Therefore, the web is slender

$R_{pw} := 1$ For slender webs

$$R_{pg} := \min\left[1, 1 - \frac{a_w}{1200 + 300 \cdot a_w} \cdot \left(2 \cdot \frac{D_{cy}}{t_w} - \lambda_{rw.AISC2016}\right)\right] = 0.971$$

Flange Local Buckling Parameters

$\lambda_f = 18$ $\lambda_{pf} = 8.354$ Calculated previously

$$k_c := \max\left(\min\left(\frac{4}{\sqrt{\frac{h}{t_w}}}, 0.76\right), 0.353\right) = 0.353$$

$$\lambda_{rf.AISC2016} := 0.95 \cdot \sqrt{\frac{k_c \cdot E}{0.7 F_y}} = 14.832$$

$\lambda_f > \lambda_{rf.AISC2016} = 1$ Therefore, flange is slender

FLB Strength

$$M_{nFLB} := \frac{0.9 \cdot R_{pg} \cdot E \cdot k_c \cdot S_x}{\lambda_f^{\,2}} = 2.403 \times 10^3 \cdot kip \cdot in$$ For slender flange

LTB Strength

$L_b = 210 \cdot in$ Given unbraced length

$$L_p := 1.1 \cdot r_{te} \cdot \sqrt{\frac{E}{F_y}} = 53.681 \cdot in$$

$$L_r := \pi \cdot r_{te} \cdot \sqrt{\frac{E \cdot S_x}{0.7 \cdot M_{yc}}} = 183.244 in$$ J=0 since the web is slender

$L_p < L_r < L_b = 1$ Section has a slender unbraced length

Calculating LTB strength for gross area:

$$M_{nLTB} := \min\left[\frac{C_b \cdot R_{pg} \cdot \pi^2 \cdot E \cdot S_x}{\left(\frac{L_b}{r_{te}}\right)^2}, R_{pg} \cdot R_{pc} \cdot M_{yc}\right] = 2.703 \times 10^3 \cdot kip \cdot in$$

Strength of Section

$$M_n := \min\left(M_{nFLB}, M_{nLTB}\right) = 2.403 \times 10^3 \cdot kip \cdot in$$

APPENDIX C. ALTERNATE RECOMMENDED "FPB-NLG-II" PROCEDURE

The "FPB-NLG-II" procedure is very similar to the "FPB-NLG" procedure outlined in Chapter 2. This procedure recognizes the slender flange post-buckling resistance but does not account for the presence of any local-global buckling interaction. This means, the global LTB strength is based on gross section properties, i.e., it is assumed that the premature buckling of slender flanges does not impact the global buckling strength.

The slender flange post-buckling resistance is accounted for using the effective width method. However, contrary to FPB-NLG, the FPB-NLG-II procedure recommends using the yield stress of the compression flange, F_{yc}, in the effective width equation (see Equation 1 repeated below) instead of the overall buckling stress $F_{ngLTB} = (M_{ngLTB}/S_{xc} \leq F_{yc})$ used in Equation 5 for the FPB-NLG procedure.

$$b_e = \min\left[b_{fc}\left(1 - 0.22\sqrt{\frac{F_{el}}{F_{yc}}}\right)\sqrt{\frac{F_{el}}{F_{yc}}}, b_{fc} \right]$$

In this equation,

$$F_{el} = \frac{0.9Ek_c}{\lambda_f^{\,2}}$$

This approach simplifies the calculation of FLB resistance. The plots for test Cases 1 through 5 from Section 3.3 are presented in Figures 42 through 46 below for the FPB-

NLG-II and FPB-NLG procedures. The solid markers in these plots represent an LTB failure while the hollow markers represent an FLB failure mode of members.

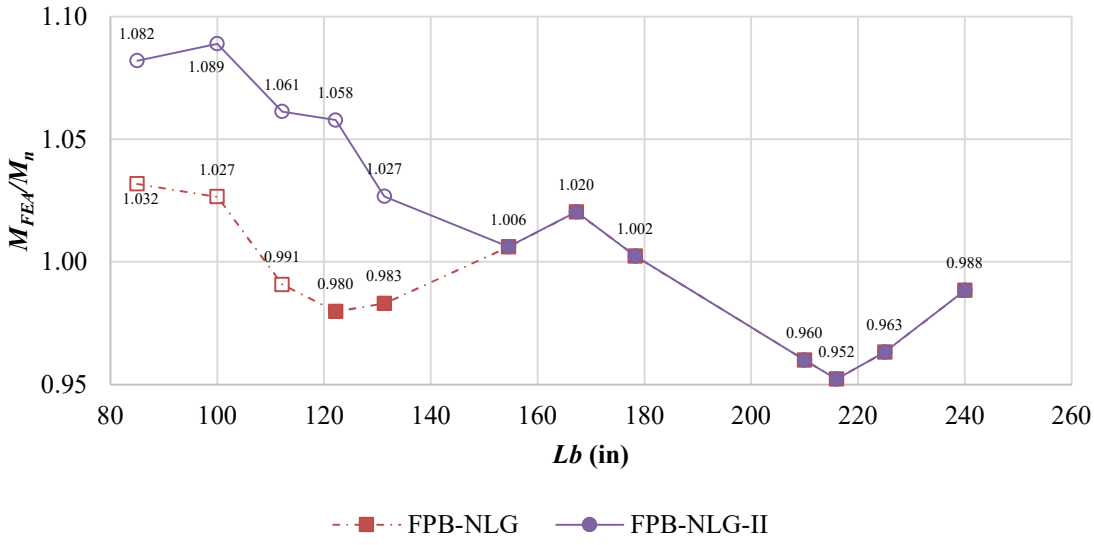

Figure 42: Comparison of M_{FEA}/M_n for the FPB-NLG and FPB-NLG-II procedures considered for Case 1 test members (slender-flange – slender-web sections under uniform moment loading having F_y = 60 ksi)

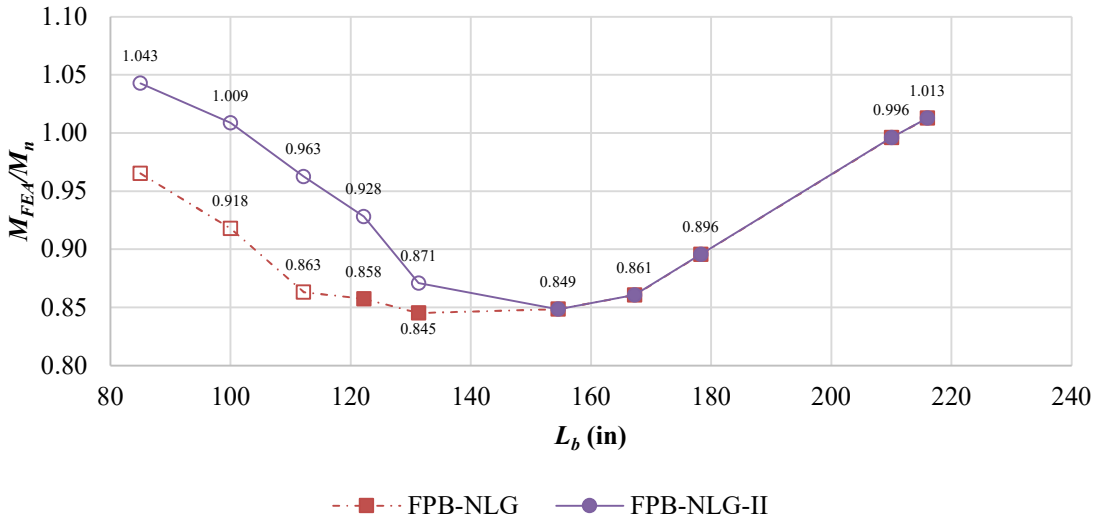

Figure 43: Comparison of M_{FEA}/M_n for the FPB-NLG and FPB-NLG-II procedures considered for Case 2 test members (slender-flange – slender-web sections under uniform moment loading having F_y = 100 ksi)

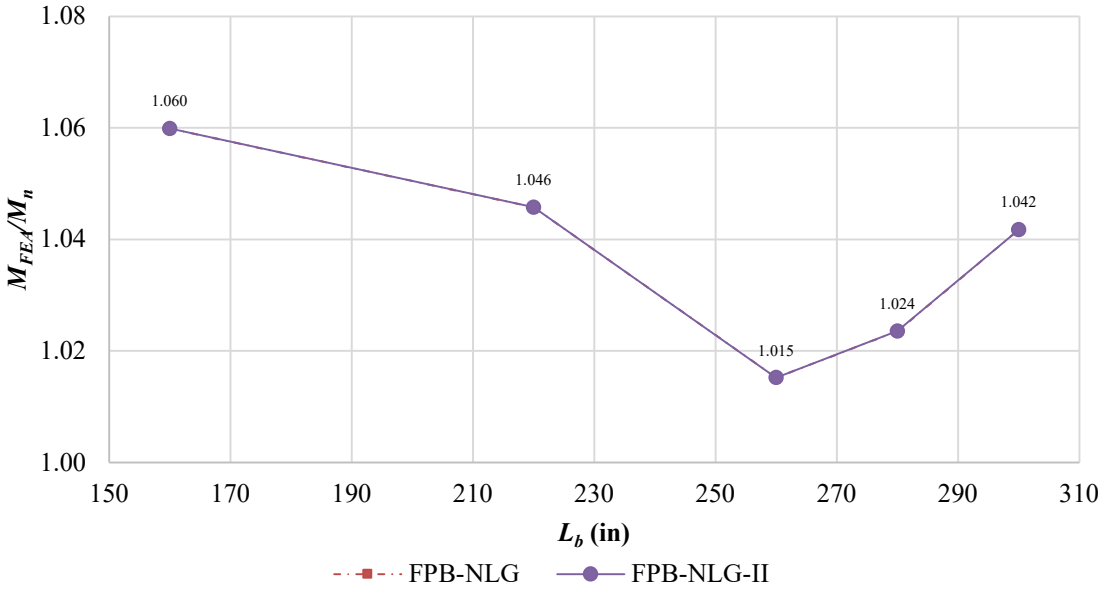

Figure 44: Comparison of M_{FEA}/M_n for the FPB-NLG and FPB-NLG-II procedures considered for Case 3 test members (slender flange – compact web sections under uniform moment loading having F_y = 60 ksi)

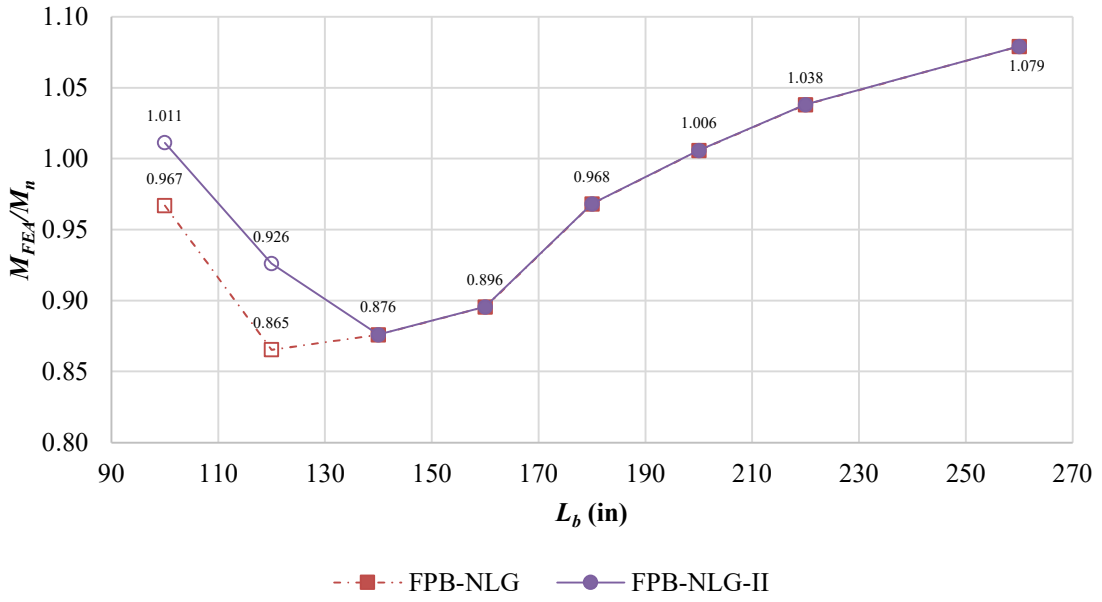

Figure 45: Comparison of M_{FEA}/M_n for the FPB-NLG and FPB-NLG-II procedures considered for Case 4 test members (slender-flange – compact-web sections under uniform moment loading having F_y = 100 ksi)

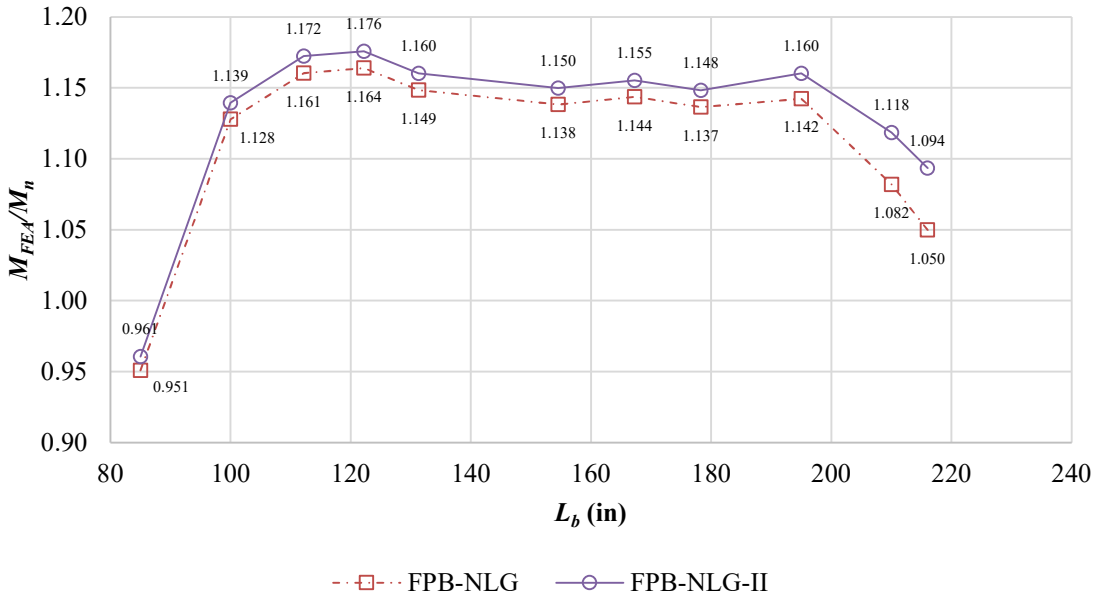

Figure 46: Comparison of M_{FEA}/M_n for the FPB-NLG and FPB-NLG-II procedures considered for Case 5 test members (slender-flange – slender-web sections under a linear moment gradient having F_y = 60 ksi)

Figures 42 through 46 show that the strength predictions by FPB-NLG-II procedure are slighly more conservative than the FPB-NLG procedure for sections failing in FLB mode, shown by empty markers on the plots. This is because the FPB-NLG procedure uses an overall buckling stress in the effective width calculation. For these members, the overall buckling stress is lower than the yield stress, F_y, used in the effective width equation of FPB-NLG-II procedure. The use of a more damning stress in the effective width equation results in a smaller effective width, therefore, a more conservative strength prediction. The strength predictions in Figures 42 through 46 converge to one another for longer unbraced lengths where LTB failure mode governs.

APPENDIX D. VALIDATION OF FINITE ELEMENT ANALYSIS PROCEDURES

In this appendix, representative test models based on the finite element analysis procedure presented in Chapter 4 are subjected to a validation study to assess the adequacy of the procedure and the impact of various parameters. As part of the validation study, an experimental test conducted by Basler et al. (1960) is modeled using the finite element analysis procedures discussed in Chapter 4. In addition, a sensitivity analysis is conducted on selected test members to study the impact of variation in geometric imperfections and residual stresses.

D1. Validation of Finite Element Analysis by Comparison to an Experiment

One of the experimental tests conducted by Basler et al. (1960), named G1-T1, is selected for the validation study. This is a hybrid strength and singly-symmetric test member with a highly slender compression flange ($b_f/2t_f$ = 24) and a slender web. The test set-up is shown in Figure 47 (White and Jung, 2004) and the cross-section dimension are given in Table 3.

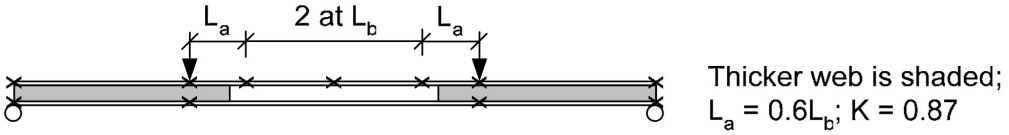

Figure 47: Load and boundary conditions of the experimental test conducted by Basler et al. (1960) selected for FEA validation study (White and Jung, 2004)

The total length of the test member in Figure 47 is 45 ft. Lengths L_b and L_a correspond to 6.25 ft and 3.75 ft respectively. The yield stresses of the compression flange, tension flange and web are 35.4 ksi, 35.8 ksi and 33 ksi respectively. It is noted that the web thickness of the shaded region (Figure 47) is greater than the middle unshaded region possibly to prevent shear failure of the test section at the end spans. However, the value of increased web thickness, as well as the span of the shaded region, are not known from the experimental documentation. The web thickness is modeled the same as in the main test section in this region.

Table 3: Dimensions of the experimental test section (Basler et al., 1960) selected for FEA validation study ($b_{fc}/2t_{fc}$ = 24, h/tw = 185.2)

Test Name	h (in)	t_w (in)	b_{fc} (in)	t_{fc} (in)	b_{ft} (in)	t_{ft} (in)
G1-T1	50	0.270	20.56	0.427	12.25	0.76

The finite element model replicates the test set up of Figure 47. Lateral braces are provided at the points marked with cross signs in Figure 47 and transverse stiffeners are provided at the load points and end-supports. The web is modelled with 50 elements along the web depth while the flanges are modelled with 12 elements along the flange width. The finite element analysis is conducted using the recommended values of residual stresses and geometric imperfections in Sections 4.3 and 4.4. It is observed that the FEA strength prediction is 11.7% greater than the reported experimental strength by Basler et al (1960). A scaled deformed shape of this test member at peak load plotted with the von Misses

stress field at the top surface of shell elements is shown in Figure 48. It can be seen that the slender compression flange shows significant distortion at failure.

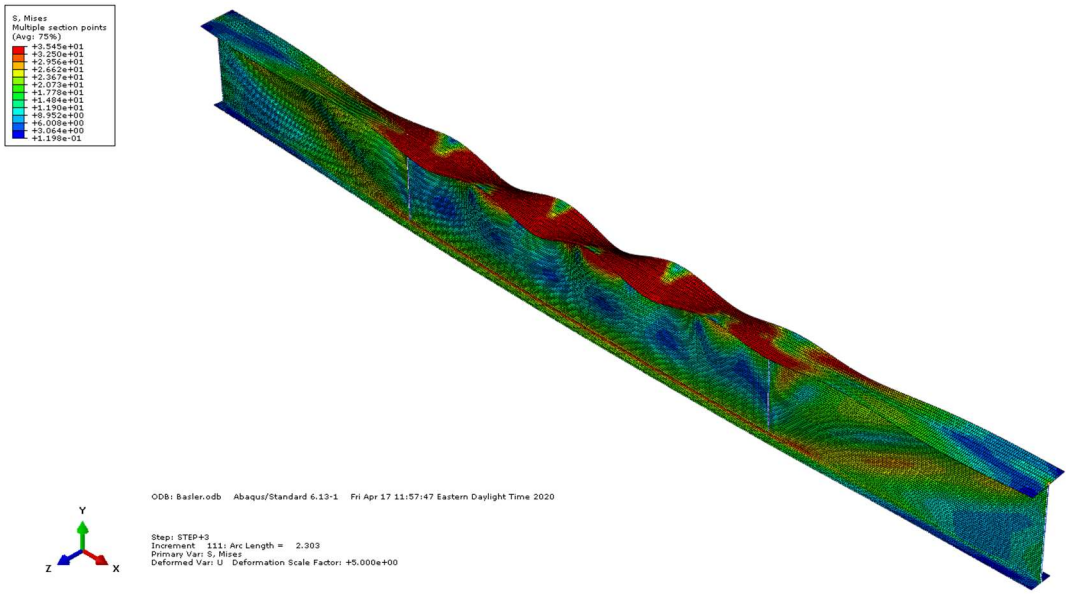

Figure 48: Deformed shape of G1-T1 test member (Basler et al., 1960) at peak load plotted with von Mises stress contours (displacement scale factor = 5.0)

Another FEA analysis of this test is conducted using the full "Best-fit Prawel" residual stress pattern, including the web residual stresses, and full geometric imperfections in contrast to Sections 4.3 and 4.4 which recommend half values. This test yields an 8% higher FEA strength prediction compared to the reported experimental strength.

D2. Validation of Finite Element Analysis via Sensitivity Studies

A sensitivity study is conducted to note the impact of the magnitude of geometric imperfections and residual stresses on the strength predictions by FEA tests. The following three sections are selected for this study:

1. Test member CW-18 from Table 1 in Chapter 3. This is a 60 ksi homogenous section with an unbraced length L_b = 25 in < L_p such that the failure mode is governed by FLB.
2. Test member UM-LB216-18-SW-60 from Table 2 in Chapter 3. This is a 60 ksi homogenous section.
3. Test member UM-LB154-18-SW-100 from Table 2 in Chapter 3. This is a 100 ksi homogenous section.

Test members UM-LB216-18-SW-60 and UM-LB154-18-SW-100 are selected for the sensitivity study since these are considered susceptible to local-global interaction in view of results presented in Section 5.2 in Chapter 5. The plots presented in Figures 49 through 51 show the ratio of FEA simulation strengths, M_{FEA}, over the plastic moment capacity, M_p, of the section. The naming scheme for the different conditions of geometric imperfections and residual stresses is defined as following:

- HI: Stands for "Half imperfections" wherein geometric imperfection are scaled to one-half the tolerance values as explained in Section 4.3.
- HI(-ve): Stands for "Half imperfections having local imperfections in the reverse direction" while the flange sweep imperfection remains in the same direction.
- FI: Stands for "Full imperfections", i.e., the geometric imperfections are scaled to full tolerance values.
- HR (W=0): Stands for "Half residual stresses in the flange and zero residual stresses in the web". This is the residual stress pattern recommended in Section 4.2.

- FR (W=0): Stands for “Full residual stresses in the flange and zero residual stresses in the web”
- HR (W): Stands for “Half residual stresses in the flanges and the web”
- FR (W): Stands for “Full residual stresses in the flanges and the web”

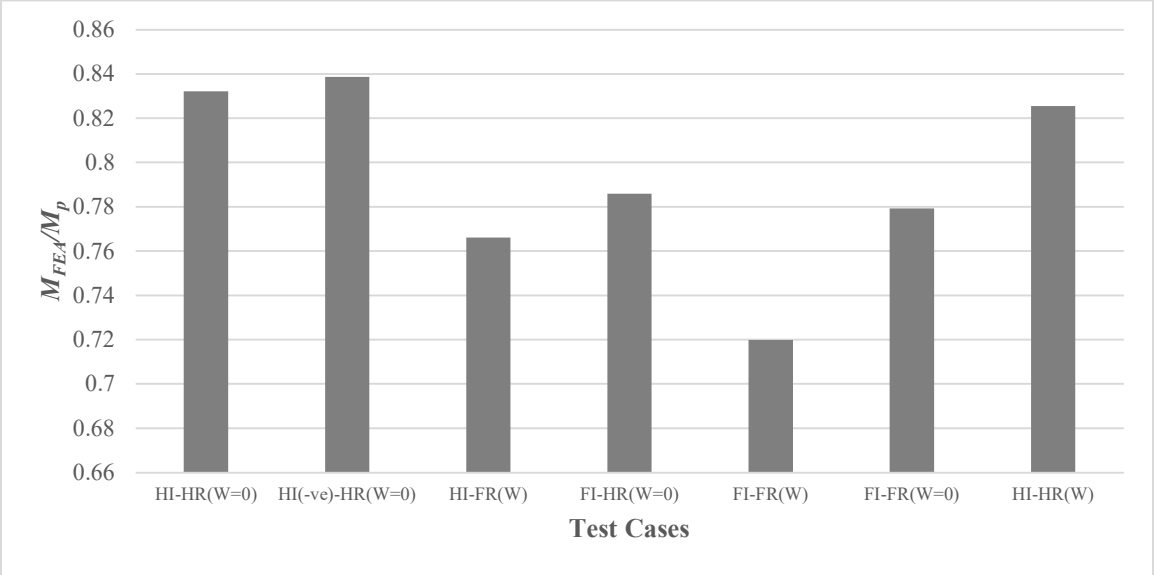

Figure 49: Comparison of M_{FEA}/M_p for test section CW-18 for different conditions of geometric imperfections and residual stress patterns

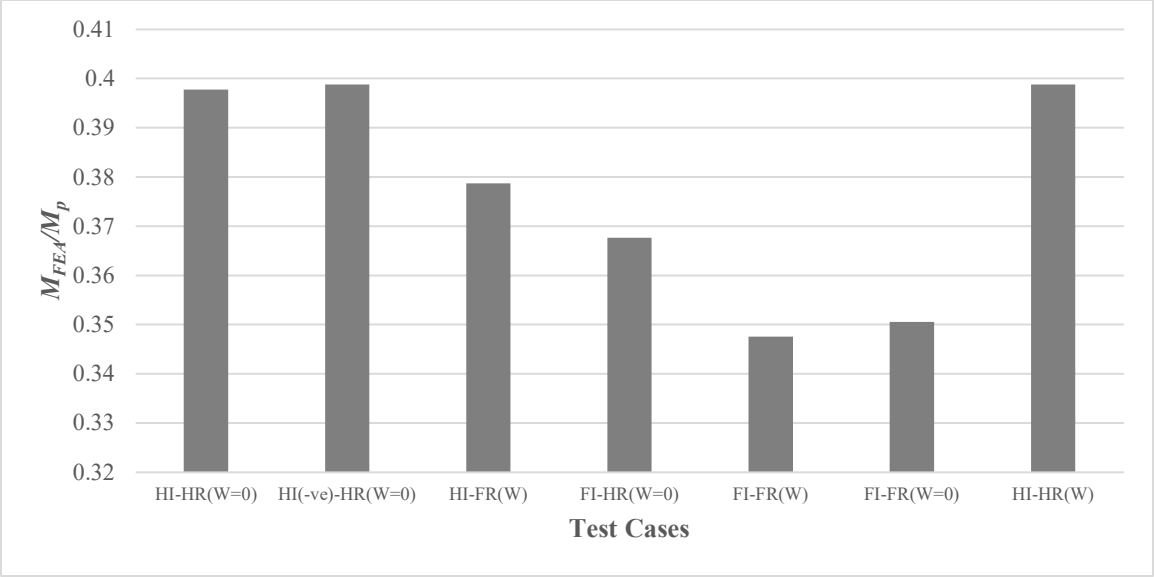

Figure 50: Comparison of M_{FEA}/M_p for test section UM-LB216-18-SW-60 for different conditions of geometric imperfections and residual stress patterns

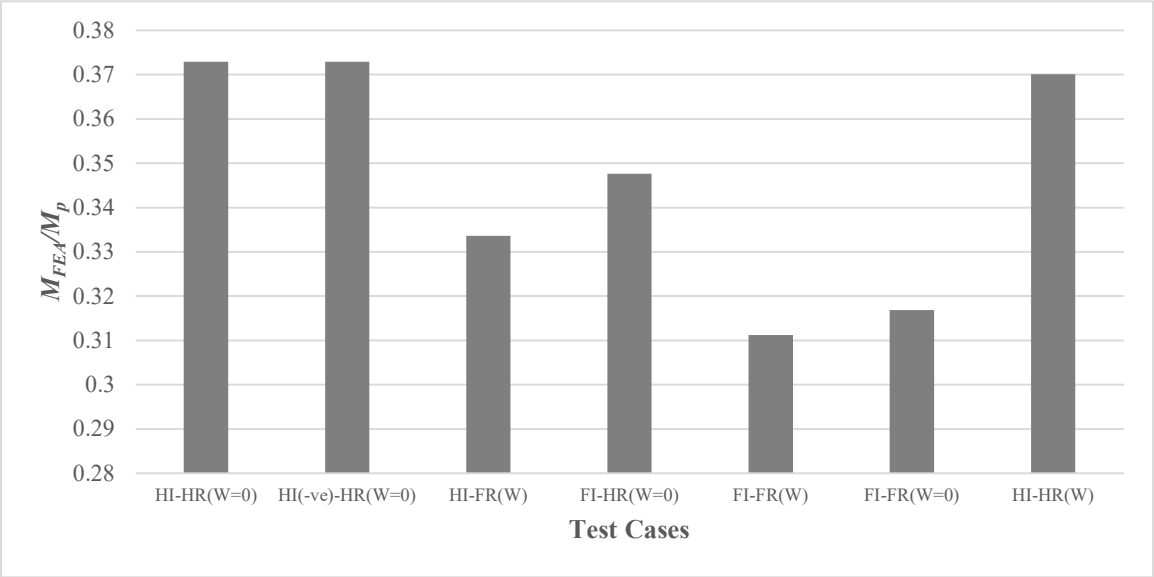

Figure 51: Comparison of M_{FEA}/M_p for test section UM-LB154-18-SW-100 for different conditions of geometric imperfections and residual stress patterns

The plots in Figures 49 through 51 show similar trend of strength predictions for all three test members for the different cases studied. It is observed that the largest reduction

in strength comes from increasing either or both the magnitudes of geometric imperfections and residual stresses. The lowest predictions for all members comes from the "FI - FR (W)" case employing the geometric imperfections with full tolerance values and the "Best-fit Prawel" residual stress pattern. It is noted that the addition of residual stresses in the web results in only a small reduction in strength predictions. The "HI(-ve) – HR (W=0)" case shows a slight increase in the strength prediction compared to the "HI – HR(W=0)". This is because the local geometric imperfections employed in the reverse direction are "helping" the member strength.

REFERENCES

AASHTO. (2017). AASHTO LRFD Bridge Design Specifications 8th Edition. *American Association of State Highway and Transportation Officials*. Washington, DC.

AISC. (2016). Code of Standard Practice for Steel Buildings and Bridges. *American Institute of Steel Construction*. Chicago, IL.

AISI. (1986). Specification for the Design of Cold-Formed Steel Structural Members, with 1989 Addendum. *American Iron and Steel Institute.* Washington, DC.

AISI. (2004). Supplement 2004 to the North American Specification for the Design of Cold-Formed Steel Structural Members, 2001 Edition, which includes: Appendix 1, Design of Cold-Formed Steel Structural Members Using Direct Strength Method. *American Iron and Steel Institute, Washington DC.*

ASCE, J. C. (1971). *Plastic Design in Steel: A Guide and Commentary.* New York, NY: American Society of Civil Engineers .

AWS. (2010). Structural Welding Code–Steel, AWS D1.1: D1.1M, 22nd ed. *AWS Committee on Structural Welding*.

Basler, K., Yen, B., Mueller, J., and Thurlimann, B. (1960). Web Buckling Tests on Welded Plate Girders. *WRC Bulletin No. 64, Welding Research Council, New York, NY*, 63.

Carskaddan, P. (1968). The bending behavior of slender-web girders with A514 steel flanges. *U.S. Steel Corporation, Applied Research, Report (57.019-904)(5)(AS-EA-23-ps)*, (p. 57).

DeWolf, J., Peköz, T., and Winter, G. (1973). Local and Overall Buckling of Cold Formed Compression Members. *Department of Structural Engineering Report, Cornell University*.

DeWolf, J., Peköz, T., and Winter, G. (1974). Local and Overall Buckling of Cold Formed Steel Members. *Journal of Structural Division, ASCE*.

Fahnestock, L. (1998). Flexural strength and ductility of HPS-100W steel I-girders. *MS Thesis, Lehigh University*.

Holtz, N., and Kulak, G. (1973). Web Slenderness Limits for Compact Beams. *Structural Engineering Report No. 43*, (p. 41). Univ. of Alberta, Alberta, Canada.

Holtz, N., and Kulak, G. (1975). Web Slenderness Limits for Noncompact Beams. *Structural Engineering Report No. 51*, (p. 21). Univ. of Alberta, Alberta, Canada.

Johnson, D. (1985). An investigation into the interaction of flanges and webs in wide flange shapes . *Annual Technical Session, Structural Stability Research Council*, (pp. 395-405).

Kalyanaraman, V., Peköz, T., and Winter, G. (1972). Performance of Unstiffened Compression Members. *Department of Structural Engineering Report, Cornell University*.

Kim, Y. D. (2010). Behavior and Design of Metal Building Frames Using General Prismatic and Web-Tapered Steel I-Section Members. *Doctoral Dissertation*. Georgia Institute of Technology.

Lew, H., and Toprac, A. (1968). The Static Strength of Hybrid Plate Girders. *S.F.R.L. Tech Rept. P550-11*, (p. 187). Structures Fatigue Research Laboratory, Dept. of Civil Engineering, Univ. of Texas, Austin, TX.

Peköz, T. (1986). Development of a unified approach to the design of cold-formed steel members. *Report SG-86-4, Ameican Iron and Steel Institute* .

Schafer, B., Fraser, T., Goel, S., McManus, P., Sherman, D., Sabol, T., . . . Leu, B. (2020). *Task Group Report on Local Buckling (Width-to-thickness) Limits.* AISC.

Seif, M. (2010). Cross-section stability of structural steel. *Doctoral Dissertation*. John Hopkins University.

Seif, M., and Schafer, B. W. (2010). Local buckling of structural steel shapes. *Journal of Constructional Steel Research*, 1232-1247.

Simulia. (2013). ABAQUS/Standard Version 6.13-1. Providence, RI, Simulia, Inc.

Subramanian, L. (2015). Flexural Resistance of Longitudinally Stiffened Plate. *Doctoral Dissertation*. Georgia Institute of Technology, Atlanta, GA.

Subramanian, L., and White, D. (2017a). Resolving the Disconnect between Lateral Torsional Buckling Experimental Tests, Test Simulations, and Design Strength Equations. *Journal of Constructional Steel Research*, 331–334.

Subramanian, L., and White, D. (2017b). "Reassessment of the Lateral Torsional Buckling Resistance of I-Section Members: Uniform-Moment Studies. *Journal of Structural Engineering*.

Subramanian, L., and White, D. (2017c). "Reassessment of the Lateral Torsional Buckling Resistance of Rolled I-Section Members: Moment Gradient Tests. *Journal of Structural Engineering, 143*(4).

Subramanian, L., Jeong, W. Y., Yellepeddi, R., and White, D. W. (2018). Assessment of I-Section Member LTB Resistances Considering Experimental Test Data and Practical Inelastic Buckling Design Calculations. *Engineering Journal*, 15-44.

Togay, O. (2018). Advanced design evaluation of planar steel frames composed of general nonprismatic I-section members. *Doctoral Dissertation*. Georgia Institute of Technology.

Togay, O., and White, D. W. (2018). Toward the Recognition of Unaccounted for Flange Local Buckling and Tension Flange Yielding Resistances in the ANSI/AISC 360 Specification. *Proceedings of the Annual Stability Conference Structural Stability Research Council*.

von Karman, T., Sechler, E., and Donnell, L. (1932). The Strength of Thin Plates in Compression. *Transactions of the ASME, 54*, 53-57.

White, D., and Jeong, W. (2020). Steel Design Guide 25, Second Edition. *AISC*.

White, D., and Jung, S. (2008). Unified Flexural Resistance Equations for Stability Design of Steel I-Section Members – Uniform Bending Tests. *Journal of Structural Engineering, 134*(9), 1450-1470.

White, D., and Jung, S.-K. (2004). Unified Flexural Resistance Equations for Stability Design of Steel I-Section Members - Uniform Bending Tests. *Structural Engineering, Mechanics and Materials Report No. 04-28*.

White, D., and Kim, Y. (2008). Unified Flexural Resistance Equations for Stability Design of Steel I-Section Members – Moment Gradient Tests. *Journal of Structural Engineering, 134*(9), 1471-1486.

White, D., and Lokhande, A. (2017). A Review of Winter's Equation and Various Plate Postbuckling Resistance Approximations. *Structural Engineering Mechanics and Materials Report No. 17-04.* School of Civil and Environmental Engineering, Georgia Institute of Technology, Atlanta, GA.

Winter, G. (1947). Strength of Thin Steel Compression Flanges. *Transactions of the ASCE, Paper No. 2305, 112*, 527-576.

Winter, G. (1970). Light Gage Cold-Formed Steel Design Manual: Commentary of the 1968 Edition. *American Iron and Steel Institute.* Washington, DC.

Ziemian, R. (2010). *Guide to Stability Design Criteria for Metal Structures, 6th Ed.* John Wiley and Sons, Inc., Hoboken, NJ.